

A novel optimal transport-based approach for interpolating spectral time series

Paving the way for photometric classification of supernovae

M. Ramirez^{1,2}, G. Pignata^{3,2}, Francisco Förster^{2,4,5,6}, Santiago González-Gaitán⁷, Claudia P. Gutiérrez^{10,11}, B. Ayala^{1,2}, Guillermo Cabrera-Vives^{2,12,13}, Márcio Catelan^{2,8,9}, A. M. Muñoz Arancibia^{2,5}, and J. Pineda-García^{1,2}

¹ Instituto de Astrofísica, Departamento de Física, Facultad de Ciencias Exactas, Universidad Andres Bello, Fernandez Concha 700, Las Condes, Santiago RM, Chile.

e-mail: m.ramirezvalenzuela@andresbello.edu

² Millennium Institute of Astrophysics, Nuncio Monseñor Sotero Sanz 100, Of. 104, Providencia, Santiago, Chile.

³ Instituto de Alta Investigación, Universidad de Tarapacá, Casilla 7D, Arica, Chile.

⁴ Data and Artificial Intelligence Initiative (IDIA), Faculty of Physical and Mathematical Sciences, Universidad de Chile, Chile.

⁵ Center for Mathematical Modeling, Universidad de Chile, Beauchef 851, Santiago 8370456, Chile

⁶ Departamento de Astronomía, Universidad de Chile, Chile

⁷ CENTRA, Instituto Superior Técnico, Universidade de Lisboa, Av. Rovisco Pais 1, 1049-001 Lisboa, Portugal.

⁸ Instituto de Astrofísica, Pontificia Universidad Católica de Chile, Av. Vicuña Mackenna 4860, 7820436 Macul, Santiago, Chile.

⁹ Centro de Astroingeniería, Pontificia Universidad Católica de Chile, Av. Vicuña Mackenna 4860, 7820436 Macul, Santiago, Chile.

¹⁰ Institut d'Estudis Espacials de Catalunya (IEEC), Gran Capità, 2-4, Edifici Nexus, Desp. 201, E-08034 Barcelona, Spain.

¹¹ Institute of Space Sciences (ICE, CSIC), Campus UAB, Carrer de Can Magrans, s/n, E-08193 Barcelona, Spain.

¹² Department of Computer Science, Universidad de Concepción, Chile.

¹³ Data Science Unit, Universidad de Concepción, Edmundo Larenas 310, Concepción, Chile.

Received January 8, 2024; accepted September 12, 2024

ABSTRACT

Context. The *Vera C. Rubin* Observatory is set to discover 1 million supernovae (SNe) within its first operational year. Given the impracticality of spectroscopic classification at such scales, it is mandatory to develop a reliable photometric classification framework. **Aims.** This paper introduces a novel method for creating spectral time series that can be used not only to generate synthetic light curves for photometric classification, but also in applications such as K-corrections and bolometric corrections. This approach is particularly valuable in the era of large astronomical surveys, where it can significantly enhance the analysis and understanding of an increasing number of SNe, even in the absence of extensive spectroscopic data.

Methods. By employing interpolations based on optimal transport theory, starting from a spectroscopic sequence, we derive weighted average spectra with high cadence. The weights incorporate an uncertainty factor for penalizing interpolations between spectra that show significant epoch differences and lead to a poor match between the synthetic and observed photometry.

Results. Our analysis reveals that even with a phase difference of up to 40 days between pairs of spectra, optical transport can generate interpolated spectral time series that closely resemble the original ones. Synthetic photometry extracted from these spectral time series aligns well with observed photometry. The best results are achieved in the *V* band, with relative residuals of less than 10% for 87% and 84% of the data for type Ia and II, respectively. For the *B*, *g*, *R*, and *r* bands, the relative residuals are between 65% and 87% within the previously mentioned 10% threshold for both classes. The worse results correspond to the *i* and *I* bands, where, in the case of SN Ia, the values drop to 53% and 42%, respectively.

Conclusions. We introduce a new method for constructing spectral time series for individual SNe starting from a sparse spectroscopic sequence, and demonstrate its capability to produce reliable light curves that can be used for photometric classification.

Key words. methods: data analysis – methods: statistical – (Stars:) supernovae: general

1. Introduction

Supernovae (SNe) are transient astronomical events that occur during the terminal phases of stellar evolution. SNe play an important role in galactic evolution, influencing both chemical evolution and energy dynamics across galaxies (e.g., Ceverino & Klypin 2009). Additionally, due to their luminous and homogeneous intensity, type Ia SNe serve as robust distance indicators, enhancing our understanding of cosmic scales (e.g., Riess et al. 1998; Perlmutter et al. 1999; Abbott et al. 2019).

The current classification scheme of SNe is mainly based on differences in their spectra, but initially they were classified into Type I and Type II based on the presence or absence of hydrogen lines in their spectra (Minkowski 1941). Furthermore, a variety of subtypes emerge depending on the manifestation and/or strength of other chemical elements (Wheeler & Levreault 1985; Elias et al. 1985; Harkness et al. 1987; Wheeler & Harkness 1990). On one hand, Type I has been divided into Ia, Ib, and Ic, where SNe Ia show strong signatures of Si II near their peak, while SNe Ib are defined by the presence of strong He I features.

SNe Ic do not show strong lines of either He or Si II. On the other hand, a subtype of type II SNe is SN IIb, where spectra at early phases are dominated by strong H I lines, but weaken with time while He I features strengthen. Finally, the spectra of SN IIn are dominated by prominent narrow emission lines of the Balmer series at all phases. From the explosion mechanism point of view, SNe can be broadly classified into thermonuclear and core collapse (CC) explosions. Thermonuclear SN coincides with the SN Ia observational class and is believed to be the result of the thermonuclear incineration of a carbon-oxygen white dwarf in a binary system (e.g., Hoyle & Fowler 1960). On the other hand, CC explosions include all the other SN observational types mentioned above (II, IIb, IIn, Ib and Ic) and are expected to be the result of the collapse of the iron-degenerate core of a massive star ($M \gtrsim 8 M_{\odot}$) (for a review see Smartt 2009)

The Legacy Survey of Space and Time (LSST) that will be carried out by the *Vera C. Rubin Observatory* with the Simonyi Survey Telescope is projected to discover more than 10^7 SNe spanning a considerable redshift range during its ten years of operations (LSST Science Collaboration et al. 2009). Given the time investment that would be required to carry the spectroscopic classification described above on the LSST sources, the development of reliable photometric classification algorithms is fundamental. This will enable the complete realization of the enormous potential of the photometric dataset produced by current and future transient surveys. The performance of a photometric classification based on machine learning techniques (e.g., Ishida & de Souza 2013; Lochner et al. 2016; Charnock & Moss 2017; Boone 2019; Villar et al. 2019; Möller & de Boissière 2020), regardless of the specific algorithm used, strongly depends on the dataset employed for training (e.g., Richards et al. 2012; Karpenka et al. 2013; Millard & Richardson 2015). In this respect, spectro-photometric time series offer a valuable resource, as they enable the construction of synthetic light curves at various redshifts, which are ideal for use as training sets.

A key aspect of training sets is that they must be representative of the diversity of the classes that are the targets for classification. The first spectral time series were constructed by combining spectra from multiple SNe belonging to the same class. These spectral "templates" are representative of the entire class of the objects that were employed in their construction. Synthetic light curves for individual objects are then generated by warping the spectra to match their observed color. Spectral templates have been generated for Type Ia SNe (e.g., Nugent et al. 2002; Hsiao et al. 2007; Lu et al. 2023) and CC SNe (e.g., Kessler et al. 2010, 2019). Nevertheless, this approach can potentially reduce the intrinsic diversity between the members of a given class, introducing biases if the spectral templates are used to generate training sets for photometric classification. This bias is particularly important for CC SNe, because of the large heterogeneity that they display within their classes. Building up spectral time series for individual SNe belonging to a given family preserves the diversity, making them particularly suitable for generating synthetic light curves for training sets. Vincenzi et al. (2019) compiled a set of 67 spectral time-series across various SN types (II, IIn, IIb, Ib, Ic, Ic-BL), integrating photometric and spectroscopic data from the literature with Gaussian processes (GPs).

In this context, we introduce a novel method for constructing spectral time series of SNe based on optimal transport (OT) and the Wasserstein barycenter. OT theory has found large applications in a variety of scientific fields, from economics to biology, physics, data science, and machine learning. OT has also been applied in the field of astronomy. Frisch et al. (2002), for example, demonstrated that the reconstruction of the early density

fluctuations of the Universe is effectively an optimization problem, leveraging optimal mass transportation techniques. Similarly, Levy et al. (2021) advanced this field by developing a fast semi-discrete OT algorithm, providing a unique and efficient approach to modeling these early cosmic structures. Nikakhtar et al. (2022, 2023) apply OT for reconstructing biased tracers in redshift space and baryon acoustic oscillations, enhancing our understanding of the structure of the Universe. Rawson & Hultgren (2022) employ OT to interpolate high-resolution images from low-resolution data, selecting the best match through a process that optimizes for the smallest Wasserstein distance, effectively refining the interpolation into a more precise reconstruction. Here, our method utilizes well-calibrated spectro-photometric data from individual events, and is therefore a versatile, data-driven approach applicable to various types of SNe.

This paper is organized as follows: In Sect. 2 we detail the data sample and discuss our selection criteria. Section 3 is dedicated to our methodology, where we elucidate the foundations of OT. Section 4 presents the tests conducted with models and the recipe we use for the production of the spectral time series. In addition, we validate our approach with observed photometry. Finally, we summarize our findings in Sect. 5.

2. Data sample

The spectra and light curves used for this work were retrieved from the open supernova catalog (Guillochon et al. 2017), from The Weizmann Interactive Supernova Data Repository (WISEREP¹) (Yaron & Gal-Yam 2012), and from the literature. The data cleaning process is described in Appendix A.

From the whole sample, we selected SNe of type Ia and II for which photometry is available in at least two bands within the Johnson-Cousins (JC) or Sloan (SDSS) photometric systems and for which a minimum of three spectra have been obtained (at least one before maximum light in the case of type Ia SNe). These selection criteria yielded an initial sample of 458 type Ia and 138 type II SNe. We assess the calibration of the spectra by comparing the flux from synthetic photometry F_{syn} with that from observed photometry F_{obs} across as many bands as possible through the following ratio:

$$\frac{F_{syn}}{F_{obs}} = K_x, \quad (1)$$

where the K_x corresponds to a given band x . F_{syn} is calculated using the following equation:

$$F_{syn} = F_0 \frac{\int f(\lambda)R(\lambda)d\lambda}{\int R(\lambda)d\lambda}, \quad (2)$$

where $f(\lambda)$ represents the flux density of the spectrum and $R(\lambda)$ is the band response. Both of these variables are functions of the wavelength λ . F_0 is the zero point (see Appendix B). We only compute F_{syn} when at least 95% of the response band is covered by the spectrum.

F_{obs} is obtained by interpolating the observed light curve using the Automatic Loess Regression (ALR) technique as outlined in Rodríguez et al. (2019) at the corresponding spectrum date.

For each spectrum, we compute the K_x values for as many bands as possible. This allows us to rescale the spectrum against

¹ <https://www.wiserep.org/>

the photometry by dividing its flux by the median of the K_x values (\tilde{K}) and also to evaluate the quality of its calibration, computing the median absolute deviation (MAD; hereafter $MAD(K)$) of these values. As the aim of this work is to assess the performance of OT, all the results presented in this paper are based on spectra with a relative error ($MAD(K)/\tilde{K}$) of less than 10%, which make up our "golden sample." The final golden sample consists of 110 SNe Ia and 31 SNe II, which are reported in Table C.1.

3. Methodology

In this work, we employ OT to interpolate between SN spectra. Introduced by Monge (1784), OT is a mathematical framework designed to help find the most efficient way to move "mass" between different distributions, understood in this context as an abstract representation of resources, probabilities, and distributed data, which in our case are spectra. For a more detailed explanation of the computational foundations, please refer to Villani (2009), Peyré & Cuturi (2020), and Zhang et al. (2021).

Moving to the mathematical formalism, we first consider the simpler, 1D case, where we move something from position $(x_1, x_2, x_3, \dots, x_N)$ to a new location $(y_1, y_2, y_3, \dots, y_N)$. The problem is to find the optimal transport plan $T(x_i) = y_i$ that minimizes the total transportation costs C_T . The total cost is given by

$$C_T = \sum_i^N c(x_i, T(x_i)), \quad (3)$$

where c is the cost function of moving from one point to another. Equation 3 establishes that, for each transport $(x) \rightarrow (y)$, the unit cost of the transport depends on the quantity to be transported (the transportation plan), given by T , and the starting point. By adding over all possible origins and destinations, we get the total cost. With the OT plan found by minimizing Eq. 3, it is possible to construct the Wasserstein distance as in Kolouri et al. (2017). Wasserstein distance is a metric for quantifying the distance between two probability distributions, and this distance is a way of measuring how much work it takes to transform one distribution into another, also referred to as the cost of moving. The Wasserstein barycenter is then the distribution that results from minimizing the total sum of these distances (costs) to all other distributions. It is like finding a middle point, not in terms of physical distance, but in terms of how much you would have to change each distribution to reach this middle point. A parameter α , ranging from 0 to 1, is defined to control the interpolation between the two distributions. An α value of 0 interpolates entirely to the first distribution, while a value of 1 interpolates to the second one. We show a practical illustration of how OT works in Fig. 1. In the top panel, the starting and final distributions are shown in blue and red, while the Wasserstein barycenter and $L2$ are shown in green and black, respectively. The barycenter $L2$, also known as the Euclidean barycenter, is calculated as the average of each corresponding pair of points of the two distributions, that is, it provides a linear interpolation. As visible in the plot, the $L2$ barycenter results in a bimodal distribution, while the Wasserstein barycenter produces a distribution that is transitional between the initial ones. The lower panel of Fig. 1 shows the interpolation path of the Wasserstein barycenter for different weights, that is, different values of α , illustrating the transition of the interpolations from one distribution to the other.

Moving closer to the subject of this paper, in Fig. 2 we apply $L2$ and OT methods to compute interpolations among black

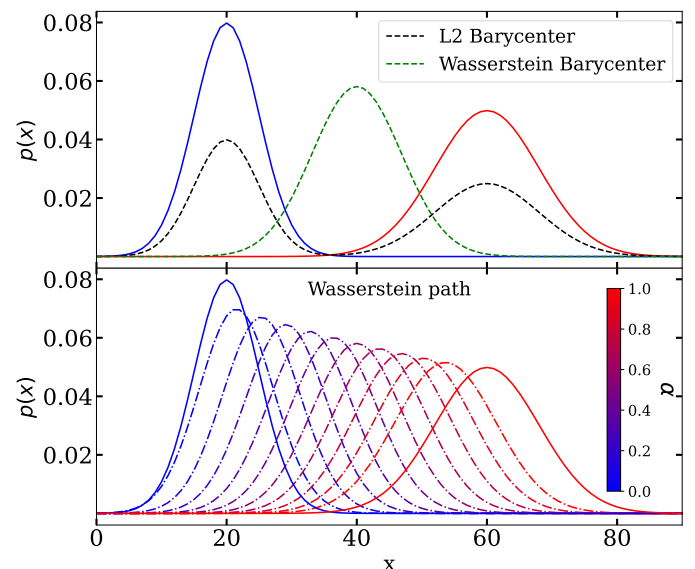


Fig. 1. Comparison between the $L2$ barycenter and the Wasserstein barycenter. The starting and final distributions are in blue and red, respectively. The black dashed distribution represents the barycenter calculated using the $L2$ distance, whereas the green dashed distribution is computed using the Wasserstein distance. The bottom panel illustrates the interpolation path of the Wasserstein barycenter for different α values, highlighting its transition from the starting distribution to the final one.

bodies. As visible in the top panel, the OT method effectively replicates the thermal evolution of black body radiation. On the contrary, the $L2$ barycenter leads to interpolations that do not accurately reflect the physical changes expected in a real black body as its temperature varies (see bottom panel).

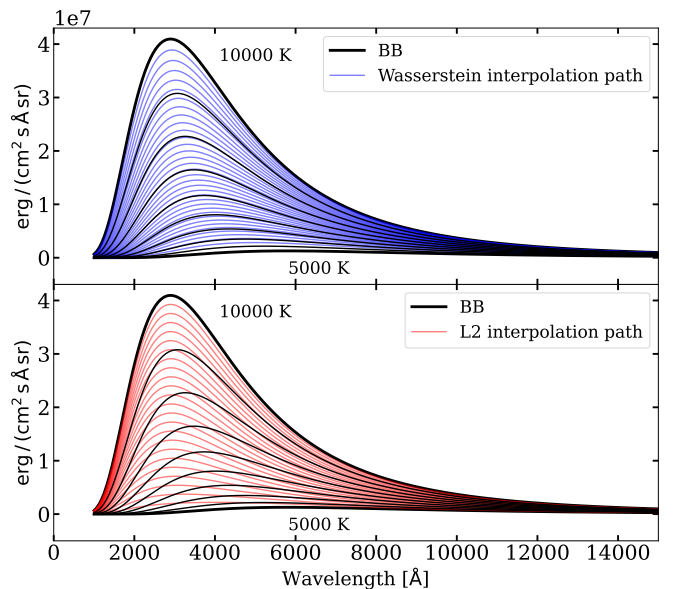


Fig. 2. Examples of black body interpolations using Wasserstein and $L2$ barycenters. In both panels, black lines show black body radiation at different temperatures. In the top panel, OT interpolations are represented in blue, while in the bottom panel, linear interpolations are presented in red.

Encouraged by these results, in this work we use the Python Optimal Transport (POT) library from Flamary et al. (2021) to

perform the interpolations in time between spectra of SNe. We specifically employ the barycenter computation function² for interpolating between two spectra, which takes a matrix A that contains the distributions, in our case the spectra, a loss matrix (M), the regularization term (reg), and the weights of each distribution. The normalized loss matrix M of size $n \times n$ was calculated with the `utils` function provided by the POT library³.

In this case, an α value of 0 interpolates entirely to the spectrum of the first date, while a value of 1 interpolates to the spectrum of the second date. Consequently, a value of 0.5 results in a spectrum interpolated exactly halfway between the two dates. Considering the scenario where the initial and final phases are given by $ph_a = 2$ and $ph_b = 6$, respectively, to interpolate to intermediate phases $ph_c = [3, 4, 5]$, α values of [0.25, 0.5, 0.75] must be employed. These α values correspond to the proportional distances of ph_c within the interval defined by ph_a and ph_b . This parameter shapes the weight array input for the `ot.bregman.barycenter()` function using the form $[1 - \alpha, \alpha]$ for the two distributions.

4. Analysis of the spectral interpolation performance

To assess the performance of OT for producing spectral time series, we conducted three sets of tests. To avoid spurious residuals introduced by the noise and miscalibration that naturally affect the observed spectra, for the first two sets of tests, we use publicly available model spectra from Dessart et al. (2014) and Dessart et al. (2013), for Type Ia and II SNe, respectively. For consistency with the tests performed on observed data, we calculated synthetic photometry for the JC and Sloan bands from the spectral time series models; this photometry is used to compute \tilde{K} and $MAD(K)$ for each interpolated spectrum. A phase to each spectrum is assigned, taking as a reference the epoch of the maximum light in the V band obtained by fitting a second-order polynomial around the peak for SNe Ia, while for SNe II we considered the midpoint of the transition phase (t_{PT}) as defined in Olivares et al. (2010).

4.1. Optimal transport on model spectra

For our purposes, the most basic form of interpolation involves pairing two spectra. Therefore, our initial set of tests focused on this procedure. The test is conducted in the following way: Let us assume we have spectra at phases ph_1 , ph_2 , and ph_3 with $ph_1 < ph_2 < ph_3$. We first interpolate a spectrum at ph_2 from the spectra at ph_1 and ph_3 ; this spectrum is then rescaled against the photometry, as detailed in Sect. 2, and compared to the actual ph_2 spectrum, computing the mean relative spectral residual, ϵ , which is defined as follows:

$$\epsilon = \frac{1}{n} \sum_{\lambda=\lambda_0}^n \left(\frac{|f_{M_\lambda} - f_{I_\lambda}|}{f_{M_\lambda}} \right), \quad (4)$$

where f_M and f_I represent the flux of the model and the flux of the interpolated spectra, respectively. This procedure is applied across all spectral pair combinations, utilizing a moving grid and progressively increasing the time interval between them.

As mentioned in Sect. 3, OT employs an α value to define the position of the interpolation, which in this study corresponds

to the phase of the spectrum we aim to compare with. It is worth mentioning that we only test interpolations with an α value ranging from 0.45 to 0.55. This is because an α of 0.5 is the most challenging case to interpolate, given that it represents the largest phase distance from the two spectra. For comparison, we also compute the same interpolations between the same pairs of spectra but employ standard linear interpolation. The results of this first set of tests can be seen in Fig. 3, where we indicate with Δ_{ph} the phase difference between the pair of spectra. As expected, for small Δ_{ph} , the relative spectral residual is low for both interpolation methods. OT shows a slower increase in ϵ , which remains below 10% even for phase gaps of 40 days for type II and 25 days for type Ia SNe. In contrast, linear interpolation sees a faster increase in ϵ , exceeding 40% as phase gaps become larger. To account for the increment of ϵ introduced by an increasing Δ_{ph} between spectra, we fit a plane in the $\Delta_{ph} - ph - \epsilon$ space for both SNe Ia and SNe II. This plane allows us to assign an uncertainty $\Sigma(\epsilon)$, which we use to penalize interpolation between pairs of spectra with large Δ_{ph} .

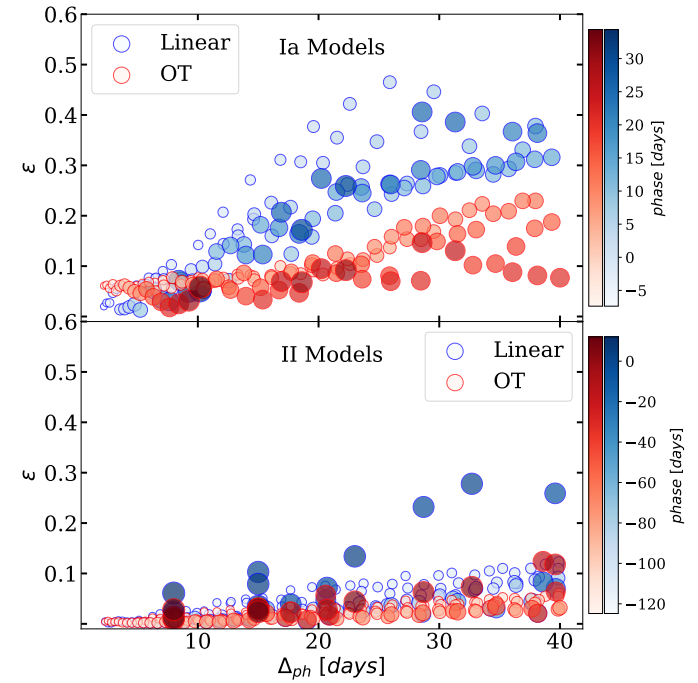


Fig. 3. Relative spectral residuals ϵ as a function of Δ_{ph} . Blue circles correspond to the linear interpolation and the red ones to the OT. The size and darkness of the circles increase with the phase of the interpolated spectrum.

In the second set of tests, to include as much information as possible in generating a given interpolated spectrum, we consider not just one pair of spectra, but all possible combinations of pairs between four spectra. This approach is applied to both the linear and the OT method, ensuring that the same information is used in both cases. While a larger number of spectra could enhance the interpolation by providing more information, this scenario is not often realistic, given that not all SNe have an extensive number of available and well-calibrated spectra. The iterative procedure is illustrated in Fig. 4, where the black boxes represent the four spectra used in the interpolation, and the white boxes indicate the position of the spectrum being interpolated. Colored lines connect the pairs of spectra used to compute the interpolated one. As in the previous test, following interpolation, we rescale the spectra against the photometry. If there are

² https://pythonot.github.io/gen_modules/ot.bregman

³ https://pythonot.github.io/gen_modules/ot.utils.html

three connections, this means that the weighted average spectrum is computed with these three interpolated spectra. As illustrated, once all possible interpolations among the existing spectrum pairs are completed, the grid moves to include an additional spectrum in the interpolation process, a concept exemplified in cycle 4.

The flux of the final spectrum $\overline{f(\lambda)}$ is computed as a weighted average over all the interpolated spectra, as follows:

$$\overline{f(\lambda)} = \frac{\sum_{i=1}^n \frac{f_i(\lambda)}{(MAD(K)_i^2 + \Sigma(\epsilon)_i^2)}}{\sum_{i=1}^n \frac{1}{(MAD(K)_i^2 + \Sigma(\epsilon)_i^2)}}, \quad (5)$$

where $f_i(\lambda)$ is the flux for the different spectra for a given λ and $MAD(K)$ has the same meaning as in Sect. 2.

The results of this second set of tests are displayed in Fig. 5, where the red circles represent the relative spectral residuals for OT interpolation and the blue circles represent those for the linear interpolation. As in Fig. 3, the size of the circles increases with phase. As expected, the residuals of the weighted spectra are larger than in Fig. 3 at a given Δ_{ph} . This is because the weighted average includes spectra with larger Δ_{ph} than in Fig. 3. However, the inclusion of more than one pair of spectra in computing the interpolated spectrum is crucial in the case of observed spectra because it reduces the effect of noise and miscalibration.

4.2. Optimal transport on observed spectra

To evaluate the performance of OT on observed data, we generated a set of time series from the golden sample of spectra outlined in Sect. 2. For each SN, we calculated interpolated spectra with a daily cadence from all the potential combinations of paired spectra within the sample. This implies that for a specific phase, we generate as many interpolated spectra as the number of combinations that include this phase. The process is the same as illustrated in Fig. 4; however, in this instance, we did not limit ourselves to using only four spectra. Our goal is to use as much data as possible, and so we included all spectra with Δ_{ph} shorter than 40 days. For a given epoch, for each interpolated spectrum, we compute $MAD(K)$, $\Sigma(\epsilon)$, and then rescale the spectrum using the \tilde{K} value. As the edges of spectra are usually poorly calibrated, we incorporate a weight term, $C(\lambda)$, which decreases linearly from 1 to 0 within a 50 Å window located at the boundaries of the interpolated spectrum. The flux of the combined spectrum is computed as follows:

$$\overline{f(\lambda)} = \frac{\sum_{i=1}^n \frac{f_i(\lambda)C_i(\lambda)}{(MAD(K)_i^2 + \Sigma(\epsilon)_i^2)}}{\sum_{i=1}^n \frac{C_i(\lambda)}{(MAD(K)_i^2 + \Sigma(\epsilon)_i^2)}}. \quad (6)$$

Having produced our spectral time series, examples of which are reported in Fig. 6, we proceed to compute the synthetic photometry using Eq. 2 and compare it with the observed one. This is done for those bands for which at least 95% of the total response is covered by the spectrum. Linear interpolation is applied to the resulting synthetic light curves, enabling us to evaluate F_{syn} for the corresponding F_{obs} dates. We then compute the relative photometric residuals ϕ and Φ as follows:

$$\phi = \frac{F_{syn} - F_{obs}}{F_{obs}}, \quad (7)$$

$$\Phi = \frac{F_{syn} - F_{obs}}{\sigma_{obs}}, \quad (8)$$

where σ_{obs} is the error associated with the observed flux. Figures 7 and C.1 present these results for ϕ and Φ , respectively.

We observe that the relative photometric residuals are generally below 10%, and we do not see significant differences between SN Ia and SN II types, with the only exception being the I and i bands, where residuals are much lower in the latter than the former. We believe that these larger residuals are mostly due to the difference in natural bands of the instruments with which the observed photometry was obtained. Both I and i bands include the Ca II NIR triplet feature and, especially for the I band, the red cutoff can vary significantly between imagers (e.g., Pignata et al. 2008a), including a different fraction of the P-Cygni profile. In SN Ia, the Ca II NIR triplet feature is much stronger than in SN II, which can explain the larger residuals visible in the plots. In the case of Φ , we observe similar trends. In most bands, the difference between synthetic and observed photometry falls within three times the error of the observed photometry. In the previous test, although the spectra are only scaled by a constant factor \tilde{K} , this factor still contains information from all the available photometric observations. To ensure that this information is not entering into the estimation of the relative residual for any given band, we conducted an additional test using a leave-one-out cross-validation technique. For this test, we selected only SNe with spectra covered by at least four bands. This approach allows us to compute \tilde{K} using at least three bands, even after leaving one out. For example, if we are computing the relative residual between the synthetic and observed photometry for the B band, and the available bands are $BVRI$, the scaling factor \tilde{K} is computed using only the VRI bands. The results of this test are shown in Figs. 8 and C.2. As can be seen, for some bands, the distribution of residuals became slightly wider ($BVgr$) or slightly narrower (Ri) with respect Figs. 7 and C.1, respectively. The only case where the distribution became significantly narrower is in the case of SN Ia for the I band, where the fraction of residuals below 0.1 magnitudes increased from 41.7% to 60.6%. The latter supports the hypothesis that a significant portion of the residuals in the I band are due to differences in the natural bands of the instruments used to observe the SNe, rather than to a decrease in the performance of the interpolation method within the wavelength range covered by this band. These results demonstrate that the spectral time series we generate with OT can produce accurate and reliable synthetic light curves that closely resemble the observed photometry. The performance across these different SN types is consistent, showing the versatility of our method.

5. Conclusions

In this study, we assessed the performance of the OT interpolation in producing spectral time series. Using SN models from Dessart et al. (2013) and Dessart et al. (2014), we first tested the OT interpolation between pairs of spectra, finding that even with phase differences of 40 days, the relative spectral residuals (ϵ) stay below 20% and 10% for SNe Ia and SNe II, respectively (Fig. 3). To include more information in the generation of a given interpolation, we included all possible combinations between four synthetic spectra. Again the relative spectral residuals (ϵ) stay below 20% and 10% for SN Ia and SN II, respectively

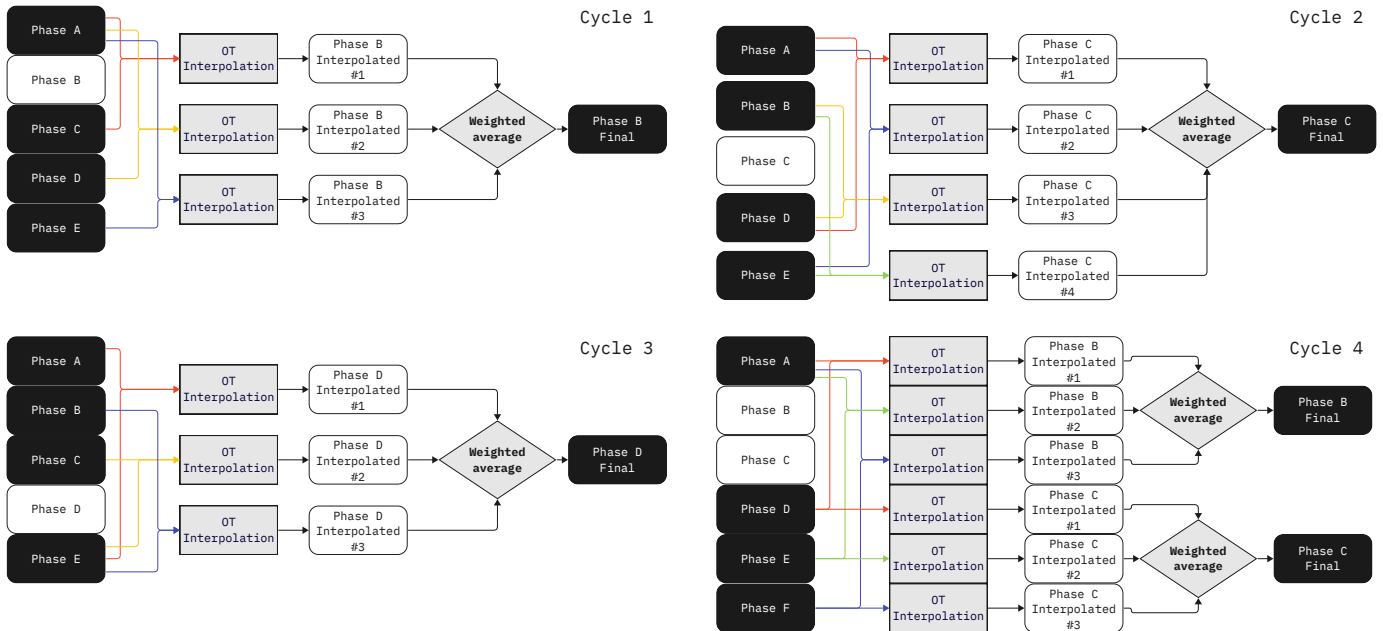


Fig. 4. Averaging scheme for the second test: Black boxes represent the spectra used for interpolation, and white boxes indicate the target phase for interpolation. Colored lines link pairs of spectra, which are used to create the interpolated spectrum at the position marked by the white box. To compute the final spectrum at a given phase, a weighted average is calculated across all interpolated spectra.

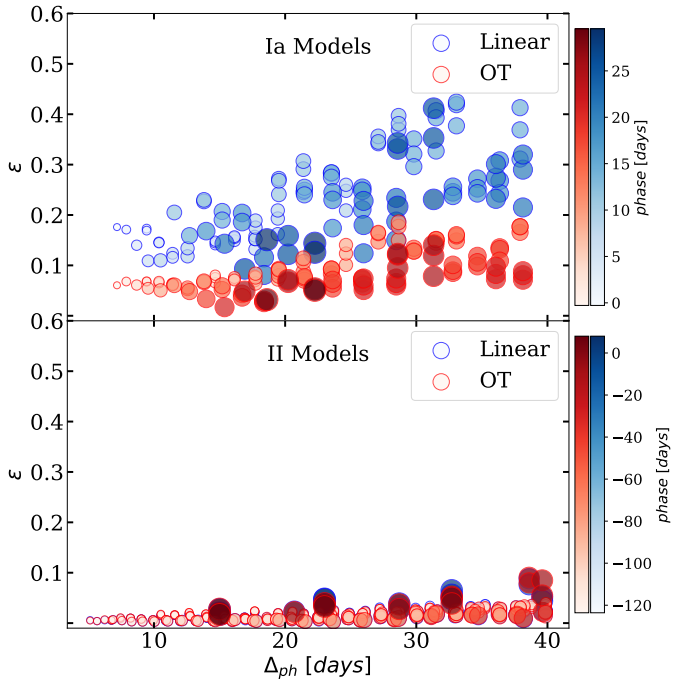


Fig. 5. Same as Fig. 3, but in this case Eq. 5 has been used to compute the flux of the spectra. We note that in this figure a given Δ_{ph} refers to the largest phase interval of the interpolated spectral pairs that enter in the weighted mean.

(Fig. 5). Our findings indicate that the error associated with the OT method increases at a slower rate with the phase difference compared to the linear method. This means that OT demonstrates a superior capability in preserving the spectral shape as the phase gap increases.

Finally, using the observed spectra of our golden sample of SNe described in Sect. 2, we computed spectral time series, from which we constructed synthetic light curves in the *BVRigri* bands. We find that a significant portion of the relative photometric residuals (ϕ) for both SN types generally fall below 10% error (Fig. 7), indicating a good match between the synthetic and observed light curves. For Type Ia SNe, this is particularly evident in the *B*, *V*, *r*, and *g* bands, while the *I* and *i* bands show more variability. Nevertheless, we find evidence that, for the *I* band, differences between the natural bands of the instruments used to observe the SNe contribute at least in part to the residuals. In the case of Type II SNe, the residuals also show a good match across all bands, with notably high percentages of residuals within acceptable error margins. When examining the residuals weighted by observational error (Φ), we observe that the majority of the differences between synthetic and observed photometry for both types of SNe are within three times the error of the observed photometry, although some specific bands for Type Ia SNe show larger deviations (Fig. C.1).

In conclusion, the OT interpolation method emerges as a robust and innovative approach for creating spectral time series; it effectively performs accurate interpolations even in scenarios with substantial phase gaps between spectra, demonstrating its capability to produce high-quality synthetic light curves. These spectral time series are highly suitable for generating training sets, which are essential for photometric classification algorithms. This aspect is particularly important in large astronomical surveys where extensive spectroscopic data may not be available. Additionally, the series may also be useful in performing K-corrections and bolometric corrections.

Acknowledgements. The authors acknowledge support from National Agency for Research and Development (ANID) grants ANID-PFCHA/Doctorado Nacional/2020-21202606 (MR), ANID-PFCHA/Doctorado Nacional/2022-21221964 (BA). Support from the Chilean Ministry of Economy, Development, and Tourism's Millennium Science Initiative through grant ICN_12009, awarded to the Millennium Institute of Astrophysics (GP, MC, AMMA, FF); by

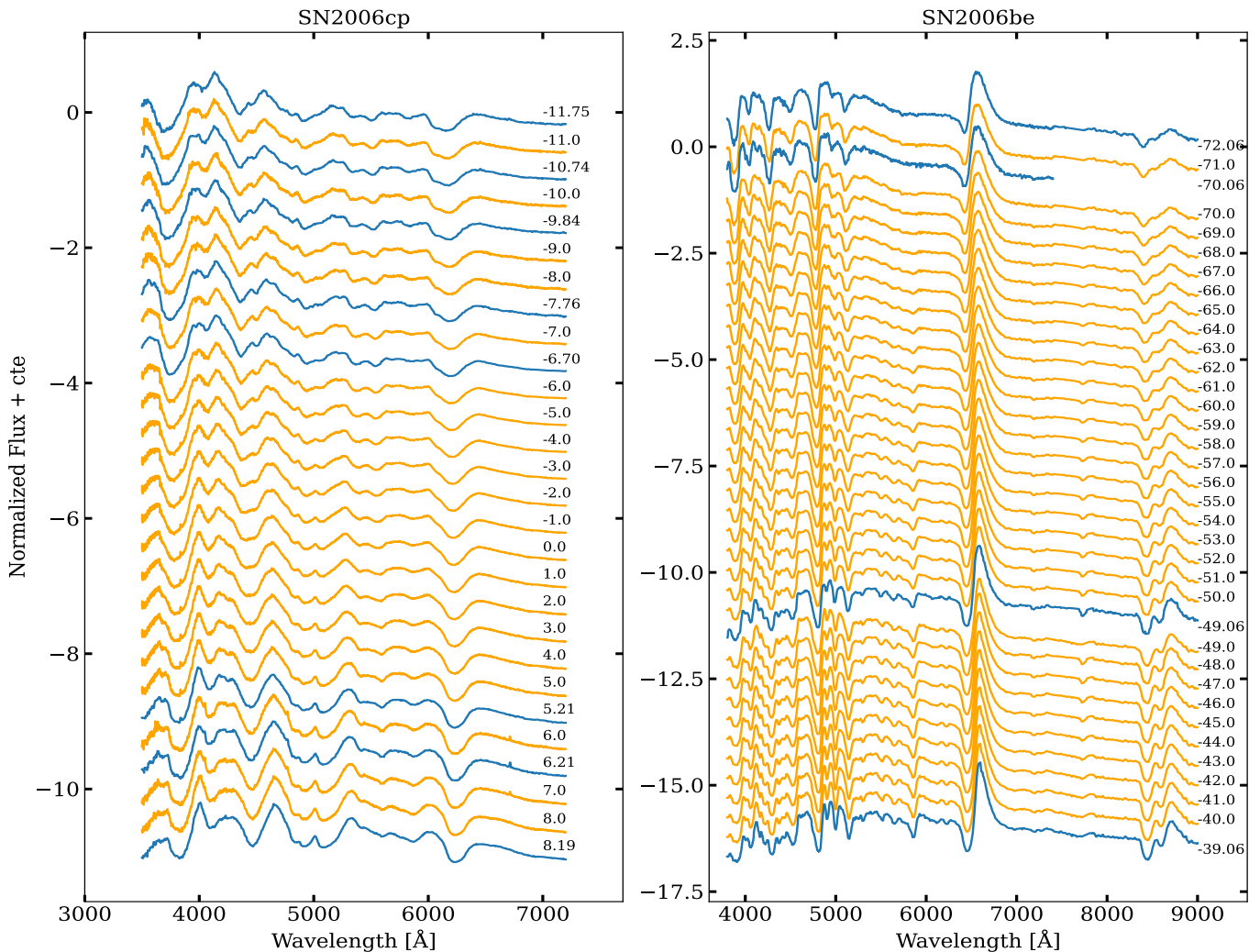


Fig. 6. Spectral time series for Type Ia SN2006cp and Type II SN2006be. The observed spectra are shown in blue, while our spectral time series, calculated with the weighted average OT, are displayed in orange. The black numbers represent the phase with respect to the maximum flux and the t_{pt} , respectively.

FONDECYT Regular grant 1231637(MC), FONDECYT Regular 1200710 (FF) and by ANID's Basal project FB210003(MC,FF). BASAL project FB210005 (AMMA), BASAL Center of Mathematical Modeling Grant PAI AFB-170001 (FF). SGG acknowledges support by FCT under Project CRISP PTDC/FIS-AST-31546/2017 and Project No. UIDB/00099/2020. CPG acknowledges financial support from the Secretary of Universities and Research (Government of Catalonia) and by the Horizon 2020 Research and Innovation Programme of the European Union under the Marie Skłodowska-Curie and the Beatriu de Pinós 2021 BP 00168 programme, from the Spanish Ministerio de Ciencia e Innovación (MCIN) and the Agencia Estatal de Investigación (AEI) 10.13039/501100011033 under the PID2020-115253GA-I00 HOSTFLOWS project, and the program Unidad de Excelencia María de Maeztu CEX2020-001058-M.

- Argo, M. K., Muxlow, T. W. B., Beswick, R. J., Pedlar, A., & Marcaide, J. M. 2004, IAU Circ., 8399, 3
 Argyle, R. W., Morrison, L. V., Knudsen, T., et al. 1994, IAU Circ., 5976, 3
 Behrend, R., Roy, R., Rinner, C., et al. 2004, IAU Circ., 8265, 2
 Benetti, S., Cappellaro, E., Turatto, M., et al. 1994, A&A, 285, 147
 Bessell, M. S., Castelli, F., & Plez, B. 1998, A&A, 333, 231
 Blondin, S., Kirshner, R., Challis, P., & Berlind, P. 2007a, Central Bureau Electronic Telegrams, 1062, 2
 Blondin, S., Kirshner, R., Challis, P., & Calkins, M. 2007b, Central Bureau Electronic Telegrams, 1048, 2
 Blondin, S., Matheson, T., Kirshner, R. P., et al. 2012, AJ, 143, 126
 Boone, K. 2019, AJ, 158, 257
 Bouma, R. J., Lehky, M., & Carvajal, J. 1998, IAU Circ., 6993, 3
 Branch, D., Garnavich, P., Matheson, T., et al. 2003, AJ, 126, 1489
 Brown, P. J., Breeveld, A. A., Holland, S., Kuin, P., & Pritchard, T. 2014, Ap&SS, 354, 89
 Brown, P. J., Dawson, K. S., Harris, D. W., et al. 2012, ApJ, 749, 18
 Bufano, F., Immler, S., Turatto, M., et al. 2009, ApJ, 700, 1456
 Burns, C. R., Parent, E., Phillips, M. M., et al. 2018, ApJ, 869, 56
 Cellier-Holzem, F., Canto, A., Antilogus, P., et al. 2012, The Astronomer's Telegram, 4566, 1
 Ceverino, D. & Klypin, A. 2009, ApJ, 695, 292
 Chakrabarti, S., Ray, A., Smith, R., et al. 2016, ApJ, 817, 22
 Charnock, T. & Moss, A. 2017, ApJ, 837, L28
 Childress, M. J., Hillier, D. J., Seitenzahl, I., et al. 2015, MNRAS, 454, 3816
 Childress, M. J., Scalzo, R. A., Sim, S. A., et al. 2013, ApJ, 770, 29
 Childress, M. J., Tucker, B. E., Yuan, F., et al. 2016, PASA, 33, e055
 Chomiuk, L., Soderberg, A. M., Chevalier, R. A., et al. 2016, ApJ, 821, 119

References

- 1997, NATO Advanced Study Institute (ASI) Series C, Vol. 486, Thermonuclear supernovae
 Abbott, T. M. C., Allam, S., Andersen, P., et al. 2019, ApJ, 872, L30
 Aldering, G., Adam, G., Antilogus, P., et al. 2002, in Society of Photo-Optical Instrumentation Engineers (SPIE) Conference Series, Vol. 4836, Survey and Other Telescope Technologies and Discoveries, ed. J. A. Tyson & S. Wolff, 61–72
 Altavilla, G., Fiorentino, G., Marconi, M., et al. 2004, MNRAS, 349, 1344
 Altavilla, G., Stehle, M., Ruiz-Lapuente, P., et al. 2007, A&A, 475, 585
 Anderson, J. P., González-Gaitán, S., Hamuy, M., et al. 2014, ApJ, 786, 67
 Andrews, J. E., Gallagher, J. S., Clayton, G. C., et al. 2010, ApJ, 715, 541

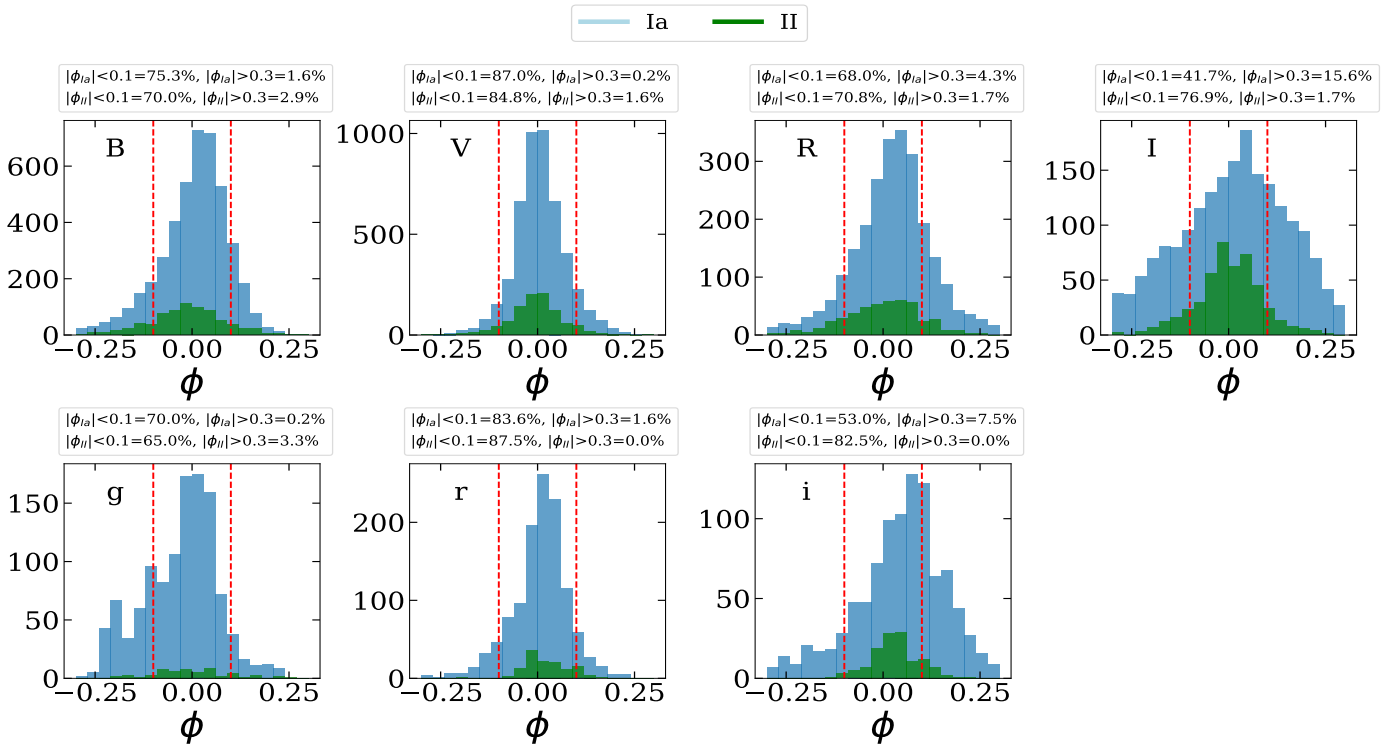


Fig. 7. Relative photometric residuals ϕ for each of the $BVR\text{I}g\text{r}i$ filters. The red dotted line denotes the zones where $|\phi| < 0.1$. The legend also includes the fraction of relative residuals that fall outside the range shown in the histogram ($|\phi| > 0.3$).

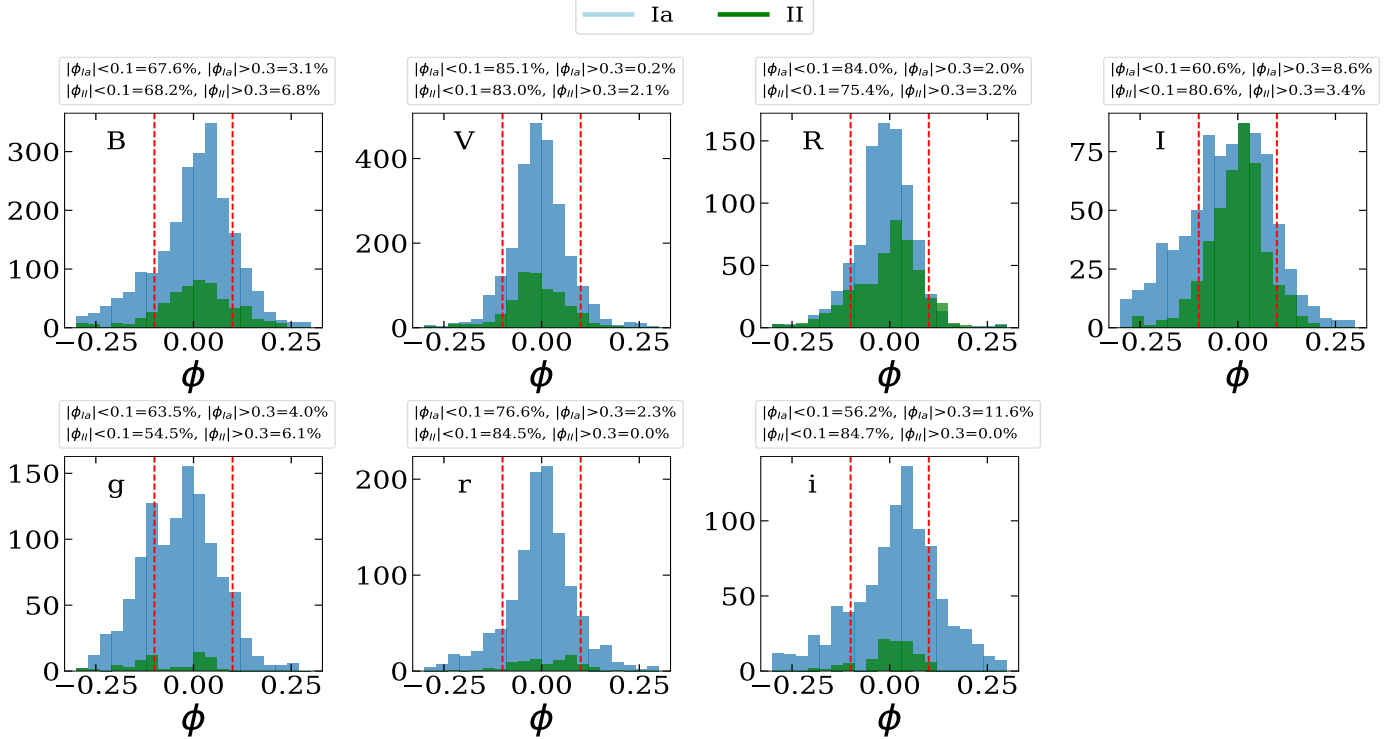


Fig. 8. Same as Fig. 7, but with the relative residuals computed using the leave-one-out cross-validation test.

- Chomiuk, L., Soderberg, A. M., Moe, M., et al. 2012, ApJ, 750, 164
 Christensen, L., Becker, T., Jahnke, K., et al. 2003, A&A, 401, 479
 Contreras, C., Hamuy, M., Phillips, M. M., et al. 2010, AJ, 139, 519
 Corelli, P., Yamaoka, H., & Itagaki, K. 2008, Central Bureau Electronic Telegrams, 1228, 2
 Cousins, A. W. J. 1980, South African Astronomical Observatory Circular, 1, 234

- Cousins, A. W. J. 1984, South African Astronomical Observatory Circular, 8, 69
 de Jaeger, T., Zheng, W., Stahl, B. E., et al. 2019, MNRAS, 490, 2799
 Dessart, L., Blondin, S., Brown, P. J., et al. 2008, ApJ, 675, 644
 Dessart, L., Blondin, S., Hillier, D. J., & Khokhlov, A. 2014, MNRAS, 441, 532
 Dessart, L., Hillier, D. J., Waldman, R., & Livne, E. 2013, Monthly Notices of the Royal Astronomical Society, 433, 1745
 Dhungana, G., Kehoe, R., Vinko, J., et al. 2016, ApJ, 822, 6

- Diepvens, A., Gonzalez, J. J., Bouma, R. J., & King, B. 2006, IAU Circ., 8766, 3
- Doi, T., Nakano, S., Itagaki, K., Naito, H., & Iizuka, R. 2007, Central Bureau Electronic Telegrams, 848, 1
- Drake, A. J., Djorgovski, S. G., Mahabal, A., et al. 2009, ApJ, 696, 870
- Elias, J. H., Matthews, K., Neugebauer, G., & Persson, S. E. 1985, ApJ, 296, 379
- Elias-Rosa, N., Benetti, S., Cappellaro, E., et al. 2006, MNRAS, 369, 1880
- Elmhamdi, A., Danziger, I. J., Chugai, N., et al. 2003, MNRAS, 338, 939
- Fabbri, J., Otsuka, M., Barlow, M. J., et al. 2011, MNRAS, 418, 1285
- Faran, T., Poznanski, D., Filippenko, A. V., et al. 2014, MNRAS, 442, 844
- Filippenko, A. V. & Foley, R. J. 2004, IAU Circ., 8453, 3
- Flamary, R., Courty, N., Gramfort, A., et al. 2021, Journal of Machine Learning Research, 22, 1
- Folatelli, G., Morell, N., Phillips, M. M., et al. 2013, ApJ, 773, 53
- Foley, R. J., Challis, P. J., Filippenko, A. V., et al. 2012, ApJ, 744, 38
- Foley, R. J., Filippenko, A. V., & Jha, S. W. 2008, ApJ, 686, 117
- Foley, R. J., Fox, O. D., McCully, C., et al. 2014, MNRAS, 443, 2887
- Foley, R. J., Scolnic, D., Rest, A., et al. 2018, MNRAS, 475, 193
- Fox, O. D., Chevalier, R. A., & Skrutskie, M. F. 2010, The Astronomer's Telegram, 2665, 1
- Fox, O. D., Filippenko, A. V., Skrutskie, M. F., et al. 2013, AJ, 146, 2
- Friedman, A. S., Wood-Vasey, W. M., Marion, G. H., et al. 2015, ApJS, 220, 9
- Frieman, J., Prasad, R. R., Li, W., et al. 2006, IAU Circ., 8754, 1
- Frieman, J. & Sloan Digital Sky Survey Collaboration, I. 2006, IAU Circ., 8770, 2
- Frisch, U., Matarrese, S., Mohayaee, R., & Sobolevski, A. 2002, Nature, 417, 260
- Fukugita, M., Ichikawa, T., Gunn, J. E., et al. 1996, AJ, 111, 1748
- Gagliano, R., Puckett, T., & Orff, T. 2009, Central Bureau Electronic Telegrams, 2005, 1
- Gal-Yam, A., Bufano, F., Barlow, T. A., et al. 2008, ApJ, 685, L117
- Galbany, L., Hamuy, M., Phillips, M. M., et al. 2016a, AJ, 151, 33
- Galbany, L., Moreno-Raya, M. E., Ruiz-Lapuente, P., et al. 2016b, MNRAS, 457, 525
- Gandhi, P., Yamanaka, M., Tanaka, M., et al. 2013, ApJ, 767, 166
- Ganeshalingam, M., Li, W., Filippenko, A. V., et al. 2010, ApJS, 190, 418
- Gómez, G. & López, R. 1998, AJ, 115, 1096
- Gómez, G. & López, R. 2000, AJ, 120, 367
- Gonzalez, J. J. 2005, IAU Circ., 8470, 3
- Goobar, A., Johansson, J., Amanullah, R., et al. 2014, ApJ, 784, L12
- Graham, M. L., Kumar, S., Hosseinzadeh, G., et al. 2017, MNRAS, 472, 3437
- Graur, O., Zurek, D., Shara, M. M., et al. 2016, ApJ, 819, 31
- Green, D. W. E. 2005, IAU Circ., 8604, 3
- Guillochon, J., Parrent, J., Kelley, L. Z., & Margutti, R. 2017, ApJ, 835, 64
- Gutiérrez, C. P., Anderson, J. P., Hamuy, M., et al. 2017, ApJ, 850, 89
- Hamuy, M., Pinto, P. A., Maza, J., et al. 2001, ApJ, 558, 615
- Hanzl, D. 1998, IAU Circ., 6978, 4
- Harkness, R. P., Wheeler, J. C., Margon, B., et al. 1987, ApJ, 317, 355
- Harutyunyan, A. H., Pfahler, P., Pastorello, A., et al. 2008, A&A, 488, 383
- Hendry, M. A., Smartt, S. J., Crockett, R. M., et al. 2006, MNRAS, 369, 1303
- Hendry, M. A., Smartt, S. J., Maund, J. R., et al. 2005, MNRAS, 359, 906
- Heraudeau, P., Prugniel, P., & Taupenas, J. 1994, IAU Circ., 5952, 3
- Hicken, M., Challis, P., Jha, S., et al. 2009, ApJ, 700, 331
- Hicken, M., Challis, P., Kirshner, R. P., et al. 2012, ApJS, 200, 12
- Hicken, M., Friedman, A. S., Blondin, S., et al. 2017, ApJS, 233, 6
- Hicken, M., Garnavich, P. M., Prieto, J. L., et al. 2007, ApJ, 669, L17
- Hoaglin, D. C. 2013, in Volume 16: How to Detect and Handle Outliers
- Holtzman, J. A., Marriner, J., Kessler, R., et al. 2008, AJ, 136, 2306
- Hoyle, F. & Fowler, W. A. 1960, ApJ, 132, 565
- Hsiao, E. Y., Conley, A., Howell, D. A., et al. 2007, ApJ, 663, 1187
- Inserra, C., Pastorello, A., Turatto, M., et al. 2013, A&A, 555, A142
- Inserra, C., Turatto, M., Pastorello, A., et al. 2011, MNRAS, 417, 261
- Ishida, E. E. O. & de Souza, R. S. 2013, MNRAS, 430, 509
- Jeffery, D. J., Leibundgut, B., Kirshner, R. P., et al. 1992, ApJ, 397, 304
- Jha, S., Kirshner, R. P., Challis, P., et al. 2006, AJ, 131, 527
- Johansson, J., Goobar, A., Kasliwal, M. M., et al. 2017, MNRAS, 466, 3442
- Karpenka, N. V., Feroz, F., & Hobson, M. P. 2013, MNRAS, 429, 1278
- Kessler, R., Bassett, B., Belov, P., et al. 2010, PASP, 122, 1415
- Kessler, R., Narayan, G., Avelino, A., et al. 2019, PASP, 131, 094501
- Kolouri, S., Park, S. R., Thorpe, M., Slepcev, D., & Rohde, G. K. 2017, IEEE Signal Processing Magazine, 34, 43
- Kotak, R., Meikle, W. P. S., Farrah, D., et al. 2009, ApJ, 704, 306
- Kotak, R., Meikle, W. P. S., Pignata, G., et al. 2005, A&A, 436, 1021
- Krisciunas, K., Hastings, N. C., Loomis, K., et al. 2000, ApJ, 539, 658
- Krisciunas, K., Phillips, M. M., Stubbs, C., et al. 2001, AJ, 122, 1616
- Krisciunas, K., Suntzeff, N. B., Candia, P., et al. 2003, AJ, 125, 166
- Krisciunas, K., Suntzeff, N. B., Phillips, M. M., et al. 2004, AJ, 128, 3034
- Lair, J. C., Leising, M. D., Milne, P. A., & Williams, G. G. 2006, AJ, 132, 2024
- Lee, E., Ponticello, N. J., & Li, W. 2005, IAU Circ., 8632, 2
- Lee, M. G., Park, C., Lee, J., et al. 1999, IAU Circ., 7237, 3
- Leonard, D. C. 2007, in American Institute of Physics Conference Series, Vol. 937, Supernova 1987A: 20 Years After: Supernovae and Gamma-Ray Bursters, ed. S. Immler, K. Weiler, & R. McCray (AIP), 311–315
- Leonard, D. C., Filippenko, A. V., Ganeshalingam, M., et al. 2006, Nature, 440, 505
- Leonard, D. C., Filippenko, A. V., Li, W., et al. 2002, AJ, 124, 2490
- Leonard, D. C., Li, W., Filippenko, A. V., Foley, R. J., & Chornock, R. 2005, ApJ, 632, 450
- Levy, B., Mohayaee, R., & von Hausegger, S. 2021, MNRAS, 506, 1165
- Li, W., Van Dyk, S. D., Filippenko, A. V., & Cuillandre, J.-C. 2005, PASP, 117, 121
- Lira, P., Suntzeff, N. B., Phillips, M. M., et al. 1998, AJ, 115, 234
- Lochner, M., McEwen, J. D., Peiris, H. V., Lahav, O., & Winter, M. K. 2016, ApJS, 225, 31
- López, R., Dominguez, I., Gímez, G., et al. 1991, in European Southern Observatory Conference and Workshop Proceedings, Vol. 37, European Southern Observatory Conference and Workshop Proceedings, 721
- LSST Science Collaboration, Abell, P. A., Allison, J., et al. 2009, arXiv e-prints, arXiv:0912.0201
- Lu, J., Hsiao, E. Y., Phillips, M. M., et al. 2023, ApJ, 948, 27
- Madison, D. R., Ponticello, N. J., Li, W., et al. 2006, IAU Circ., 8691, 2
- Maguire, K., Di Carlo, E., Smartt, S. J., et al. 2010, MNRAS, 404, 981
- Maguire, K., Jerkstrand, A., Smartt, S. J., et al. 2012, MNRAS, 420, 3451
- Maguire, K., Sullivan, M., Pan, Y. C., et al. 2014, MNRAS, 444, 3258
- Marshall, J. & Severson, S. 2022, Journal of Undergraduate Research in Physics [arXiv: 2212.06942]
- Matheson, T., Kirshner, R. P., Challis, P., et al. 2008, AJ, 135, 1598
- Mattei, J. A., Hurst, G. M., Lubbock, S., et al. 1986, IAU Circ., 4188, 1
- Mauerhan, J. C., Van Dyk, S. D., Johansson, J., et al. 2017, ApJ, 834, 118
- Mazzali, P. A., Lucy, L. B., Danziger, I. J., et al. 1993, A&A, 269, 423
- Mazzali, P. A., Sullivan, M., Hachinger, S., et al. 2014, MNRAS, 439, 1959
- McClelland, C. M., Garnavich, P. M., Milne, P. A., Shappee, B. J., & Pogge, R. W. 2013, ApJ, 767, 119
- Millard, K. & Richardson, M. 2015, Remote Sensing, 7, 8489
- Minkowski, R. 1941, PASP, 53, 224
- Möller, A. & de Boissière, T. 2020, MNRAS, 491, 4277
- Monge, G. 1784, Histoire de l'Académie Royale des Sciences (1781), 666–704
- Mukai, K. & Ishida, M. 1999, IAU Circ., 7205, 2
- Munari, U., Henden, A., Belligoli, R., et al. 2013, New A, 20, 30
- Navasardyan, H., Benetti, S., Harutyunyan, A., et al. 2006, IAU Circ., 8667, 2
- Navasardyan, H., Cappellaro, E., & Benetti, S. 2009, Central Bureau Electronic Telegrams, 1918, 2
- Newton, J., Puckett, T., & Orff, T. 2009, Central Bureau Electronic Telegrams, 1694, 1
- Nikakhtar, F., Padmanabhan, N., Lévy, B., Sheth, R. K., & Mohayaee, R. 2023, Phys. Rev. D, 108, 083534
- Nikakhtar, F., Sheth, R. K., Lévy, B., & Mohayaee, R. 2022, Phys. Rev. Lett., 129, 251101
- Nugent, P., Kim, A., & Perlmutter, S. 2002, PASP, 114, 803
- Olivares, F., Hamuy, M., Pignata, G., et al. 2010, ApJ, 715, 833
- Östman, L., Nordin, J., Goobar, A., et al. 2011, A&A, 526, A28
- Pan, Y. C., Foley, R. J., Kromer, M., et al. 2015, MNRAS, 452, 4307
- Panagia, N., Van Dyk, S. D., Weiler, K. W., et al. 2006, ApJ, 646, 369
- Pastorello, A., Mazzali, P. A., Pignata, G., et al. 2007a, MNRAS, 377, 1531
- Pastorello, A., Sauer, D., Taubenberger, S., et al. 2006, MNRAS, 370, 1752
- Pastorello, A., Taubenberger, S., Elias-Rosa, N., et al. 2007b, MNRAS, 376, 1301
- Pastorello, A., Valenti, S., Zampieri, L., et al. 2009, MNRAS, 394, 2266
- Pereira, R., Thomas, R. C., Aldering, G., et al. 2013, A&A, 554, A27
- Perlmutter, S., Aldering, G., Goldhaber, G., et al. 1999, ApJ, 517, 565
- Peyré, G. & Cuturi, M. 2020, Computational Optimal Transport
- Pignata, G., Benetti, S., Mazzali, P. A., et al. 2008a, MNRAS, 388, 971
- Pignata, G., Maza, J., Hamuy, M., et al. 2008b, Central Bureau Electronic Telegrams, 1506, 1
- Pignata, G., Patat, F., Benetti, S., et al. 2004, MNRAS, 355, 178
- Ponticello, N., Lee, E., & Li, W. 2005, IAU Circ., 8608, 2
- Prasad, R. & Li, W. 2007, Central Bureau Electronic Telegrams, 914, 1
- Puckett, T., Crowley, T., & Orff, T. 2007a, Central Bureau Electronic Telegrams, 966, 1
- Puckett, T., Gagliano, R., & Orff, T. 2008, Central Bureau Electronic Telegrams, 1243, 2
- Puckett, T., Gagliano, R., & Sehgal, A. 2007b, Central Bureau Electronic Telegrams, 803, 1
- Puckett, T., Langoussis, A., Newton, J., et al. 2006, IAU Circ., 8716, 1
- Rajala, A., Fox, D. B., & Gal-Yam, A. 2004, IAU Circ., 8386, 4
- Rawson, M. & Hultgren, J. 2022, Proceedings of the 30th European Signal Processing Conference, EUSIPCO, 2022., arXiv:2202.05354
- Rex, J., Li, W., & Filippenko, A. V. 2008, Central Bureau Electronic Telegrams, 1437, 1

- Richards, J. W., Homrighausen, D., Freeman, P. E., Schafer, C. M., & Poznanski, D. 2012, MNRAS, 419, 1121
- Richardson, D., Thomas, R. C., Casebeer, D., et al. 2001, in American Astronomical Society Meeting Abstracts, Vol. 199, American Astronomical Society Meeting Abstracts, 84.08
- Richmond, M. W., Treffers, R. R., Filippenko, A. V., et al. 1995, AJ, 109, 2121
- Riess, A. G., Filippenko, A. V., Challis, P., et al. 1998, AJ, 116, 1009
- Riess, A. G., Kirshner, R. P., Schmidt, B. P., et al. 1999, AJ, 117, 707
- Riess, A. G., Li, W., Stetson, P. B., et al. 2005, ApJ, 627, 579
- Rodriguez, O., Pignata, G., Hamuy, M., et al. 2019, MNRAS, 483, 5459
- Rostopchin, S. & Westfall, A. 2008, Central Bureau Electronic Telegrams, 1273, 2
- Rubin, A., Gal-Yam, A., De Cia, A., et al. 2016, ApJ, 820, 33
- Russell, R. W., Lynch, D. K., Kim, D. L., Hammel, H. B., & Perry, R. B. 2003, IAU Circ., 8186, 3
- Sahu, D. K., Anupama, G. C., Srividya, S., & Muneer, S. 2006, MNRAS, 372, 1315
- Sahu, D. K., Tanaka, M., Anupama, G. C., et al. 2008, ApJ, 680, 580
- Sako, M., Bassett, B., Becker, A. C., et al. 2018, PASP, 130, 064002
- Sauer, D. N., Mazzali, P. A., Blondin, S., et al. 2008, MNRAS, 391, 1605
- Schmidt, B. P., Kirshner, R. P., Schild, R., et al. 1993, AJ, 105, 2236
- Silverman, J. M., Foley, R. J., Filippenko, A. V., et al. 2012a, MNRAS, 425, 1789
- Silverman, J. M., Ganeshalingam, M., Cenko, S. B., et al. 2012b, ApJ, 756, L7
- Silverman, J. M., Ganeshalingam, M., & Filippenko, A. V. 2013a, MNRAS, 430, 1030
- Silverman, J. M., Kandrashoff, M. T., & Filippenko, A. V. 2009, Central Bureau Electronic Telegrams, 1969, 2
- Silverman, J. M., Nugent, P. E., Gal-Yam, A., et al. 2013b, ApJS, 207, 3
- Silverman, J. M., Pickett, S., Wheeler, J. C., et al. 2017, MNRAS, 467, 369
- Simon, J. D., Gal-Yam, A., Gnat, O., et al. 2009, ApJ, 702, 1157
- Simon, J. D., Gal-Yam, A., Penprase, B. E., et al. 2007, ApJ, 671, L25
- Smartt, S. J. 2009, ARA&A, 47, 63
- Smartt, S. J., Valenti, S., Fraser, M., et al. 2015, A&A, 579, A40
- Smitka, M. T., Brown, P. J., Suntzeff, N. B., et al. 2015, ApJ, 813, 30
- Shrivastav, S., Anupama, G. C., Sahu, D. K., & Ravikumar, C. D. 2017, MNRAS, 466, 2436
- Stahl, B. E., Zheng, W., de Jaeger, T., et al. 2020, MNRAS, 492, 4325
- Stahl, B. E., Zheng, W., de Jaeger, T., et al. 2019, MNRAS, 490, 3882
- Stanishev, V., Goobar, A., Benetti, S., et al. 2007, A&A, 469, 645
- Stritzinger, M., Suntzeff, N. B., Hamuy, M., et al. 2005, PASP, 117, 810
- Strolger, L. G., GOODS Treasury Team, & Hubble Higher-Z Supernova Team. 2003, IAU Circ., 8150, 4
- Sugerman, B. E. K., Ercolano, B., Barlow, M. J., et al. 2006, Science, 313, 196
- Szabó, G. M., Sárneczky, K., Vinkó, J., et al. 2003, A&A, 408, 915
- Szalai, T. & Vinkó, J. 2013, A&A, 549, A79
- Szalai, T., Zsíros, S., Fox, O. D., Pejcha, O., & Müller, T. 2019, ApJS, 241, 38
- Taddia, F. 2012, in Death of Massive Stars: Supernovae and Gamma-Ray Bursts, ed. P. Roming, N. Kawai, & E. Pian, Vol. 279, 403–404
- Taddia, F., Stritzinger, M. D., Phillips, M. M., et al. 2012a, A&A, 545, L7
- Taddia, F., Stritzinger, M. D., Sollerman, J., et al. 2012b, A&A, 537, A140
- Taubenberger, S., Benetti, S., Childress, M., et al. 2011, MNRAS, 412, 2735
- Taubenberger, S., Elias-Rosa, N., Kerzendorf, W. E., et al. 2015, MNRAS, 448, L48
- Taubenberger, S., Kromer, M., Hachinger, S., et al. 2013, MNRAS, 432, 3117
- Thomas, R. C., Aldering, G., Antilogus, P., et al. 2007, ApJ, 654, L53
- Tinyanont, S., Kasliwal, M. M., Fox, O. D., et al. 2016, ApJ, 833, 231
- Turatto, M., Cappellaro, E., Barbon, R., et al. 1990, AJ, 100, 771
- Valenti, S., Howell, D. A., Stritzinger, M. D., et al. 2016, MNRAS, 459, 3939
- Valenti, S., Sand, D., Pastorello, A., et al. 2014, MNRAS, 438, L101
- Van Dyk, S. D., Li, W., & Filippenko, A. V. 2003, PASP, 115, 1289
- Villani, C. 2009, Optimal Transport: Old and New, Grundlehren der mathematischen Wissenschaften (Berlin: Springer)
- Willar, V. A., Berger, E., Miller, G., et al. 2019, ApJ, 884, 83
- Vincenzi, M., Sullivan, M., Firth, R. E., et al. 2019, MNRAS, 489, 5802
- Vinkó, J., Bíró, I. B., Csák, B., et al. 2003, A&A, 397, 115
- Vinkó, J., Ordasi, A., Szalai, T., et al. 2018, PASP, 130, 064101
- Vinkó, J., Sárneczky, K., Balog, Z., et al. 2009, ApJ, 695, 619
- Vinkó, J., Takáts, K., Sárneczky, K., et al. 2006, MNRAS, 369, 1780
- Walker, A., Dahle, H., Midtskogen, O., Hurst, G. M., & Šekino, Y. 1994, IAU Circ., 5950, 1
- Walker, E. S., Baltay, C., Campillay, A., et al. 2015, ApJS, 219, 13
- Wang, L., Baade, D., Höflich, P., et al. 2003, ApJ, 591, 1110
- Wang, X., Li, W., Filippenko, A. V., et al. 2009, ApJ, 697, 380
- Wang, X., Li, W., Filippenko, A. V., et al. 2008, ApJ, 675, 626
- Wheeler, J. C. & Harkness, R. P. 1990, Reports on Progress in Physics, 53, 1467
- Wheeler, J. C. & Levrault, R. 1985, ApJ, 294, L17
- Whitaker, D. A. & Hayes, K. 2018, Chemometrics and Intelligent Laboratory Systems, 179, 82
- Yamanaka, M., Maeda, K., Kawabata, M., et al. 2014, ApJ, 782, L35
- Yamanaka, M., Naito, H., Kinugasa, K., et al. 2009, PASJ, 61, 713
- Yaron, O. & Gal-Yam, A. 2012, PASP, 124, 668
- Yuan, F., Jerkstrand, A., Valenti, S., et al. 2016, MNRAS, 461, 2003
- Yuan, F., Quimby, R., Chamarro, D., et al. 2008, Central Bureau Electronic Telegrams, 1314, 1
- Zanotta, M. V., Morris, C. S., & Merlin, J. C. 1986, IAU Circ., 4260, 4
- Zhai, Q., Zhang, J.-J., Wang, X.-F., et al. 2016, AJ, 151, 125
- Zhang, J., Wang, X., Mazzali, P. A., et al. 2014a, ApJ, 797, 5
- Zhang, J., Zhong, W., & Ma, P. 2021, A Review on Modern Computational Optimal Transport Methods with Applications in Biomedical Research
- Zhang, J.-J., Wang, X.-F., Bai, J.-M., et al. 2014b, AJ, 148, 1
- Zhang, T., Wang, X., Li, W., et al. 2006, AJ, 131, 2245
- Zheng, W., Filippenko, A. V., Mauerhan, J., et al. 2017, ApJ, 841, 64
- Zheng, W., Silverman, J. M., Filippenko, A. V., et al. 2013, ApJ, 778, L15

Appendix A: Data cleaning

Before interpolating the spectra, it is important to remove contaminants, including cosmic rays and features coming from sources such as H II regions or atmospheric telluric lines.

To automate the removal of cosmic ray interference from the spectral data, we developed a Python-based application called the Cosmic Ray Deleter (CRD)⁴. The CRD can identify and eliminate spikes using an algorithm founded on the method proposed by Whitaker & Hayes (2018). The z-scores tell us how far a value is from the average in units of standard deviation and is defined as follows:

$$z_i = \frac{x_i - \mu}{\sigma}, \quad (\text{A.1})$$

where μ is the mean and σ is the standard deviation of the population x_i . In this work, we use a robust statistics approach using the median M and the median absolute deviation (MAD) rather than the μ and σ as proposed by Whitaker & Hayes (2018). The authors employed a modified z-scores outlier detection technique to identify spikes:

$$z_i = 0.6745 \frac{\nabla x_i - M}{MAD}. \quad (\text{A.2})$$

Here $MAD = \text{median}(|x - M|)$, $\nabla x_i = x_i - x_{i-1}$, and the value 0.6745 corresponds to the 0.75th quartile of a normal distribution. We take the absolute value of the z-scores and select a threshold value of 3.5 as is recommended in Hoaglin (2013).

Spikes are corrected by calculating the mean values within a $2m+1$ window surrounding them, where m represents an adjustable input value that determines the window size. By default, $m=3$, but we may alter this value and the threshold to better accommodate the data.

Additionally, we have incorporated into the CRD the functionality to interactively remove cosmic rays. This allows users to input the specific wavelengths between which a spike is observed. This feature proves beneficial when dealing with particularly noisy spectra that contain numerous spikes, which may not necessarily be attributed to cosmic rays. Once the cosmic rays are detected it is removed connecting the two edges of the window with a straight line.

We visually inspected each spectrum and identified telluric lines using a reference spectrum. These lines were then removed through linear interpolation between the edges of each telluric feature.

Appendix B: Standard stars

For the calibration of F_0 in Eq. 2 we compare the synthetic photometry of three stars reported in Stritzinger et al. (2005), specifically HR0718, HR4468, and HR4963 with the observed photometry reported in Cousins (1980, 1984) for the *BVRI* bands and Fukugita et al. (1996) for the *g'r'i'* bands. For computing the synthetic photometry we use the *BVRI* and *g'r'i'* bands reported in Bessell et al. (1998) and Fukugita et al. (1996), respectively.

For each band we also computed the root mean square, mean, and relative error σ of the values obtained for the three stars, which are reported in Table B.1.

Table B.1. Mean F_0 value and relative error σ for each band.

Band	$F_0 [\text{erg cm}^{-2} \text{s}^{-1} \text{A}^{-1}]$	σ
<i>B</i>	6.460×10^{-9}	0.002
<i>V</i>	3.675×10^{-9}	0.002
<i>R</i>	2.232×10^{-9}	0.001
<i>I</i>	1.177×10^{-9}	0.005
<i>g</i>	4.791×10^{-9}	0.001
<i>r</i>	2.818×10^{-9}	0.005
<i>i</i>	1.907×10^{-9}	0.014

Appendix C: Extra figures and tables

The following figures display the weighted relative photometric residuals Φ , as referenced in Sect. 4.2. Fig. C.1 corresponds to the standard test, while Fig. C.2 shows the results using the leave-one-out cross-validation test. Table C.1 presents the final golden sample as referenced in Sect. 2

⁴ <https://github.com/mramirez/Cosmic-Ray-Deleter>

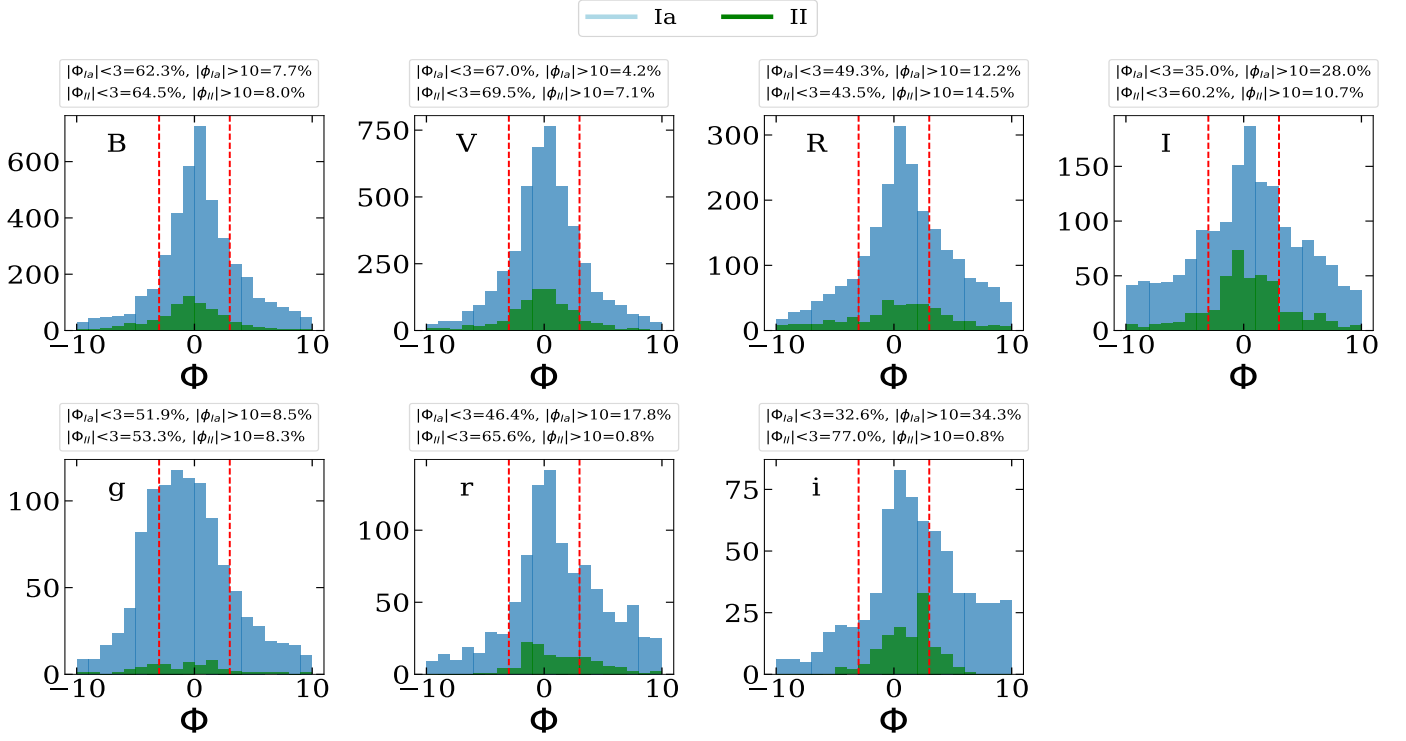


Fig. C.1. Relative photometric residuals Φ for each of the $BVRIgri$ filters. This residuals are weighted by the error in the photometry. The red dotted line denotes the zones where $|\Phi| < 3.0$. The legend also includes the fraction of relative residuals that fall outside the range shown in the histogram ($|\Phi| > 10.0$).

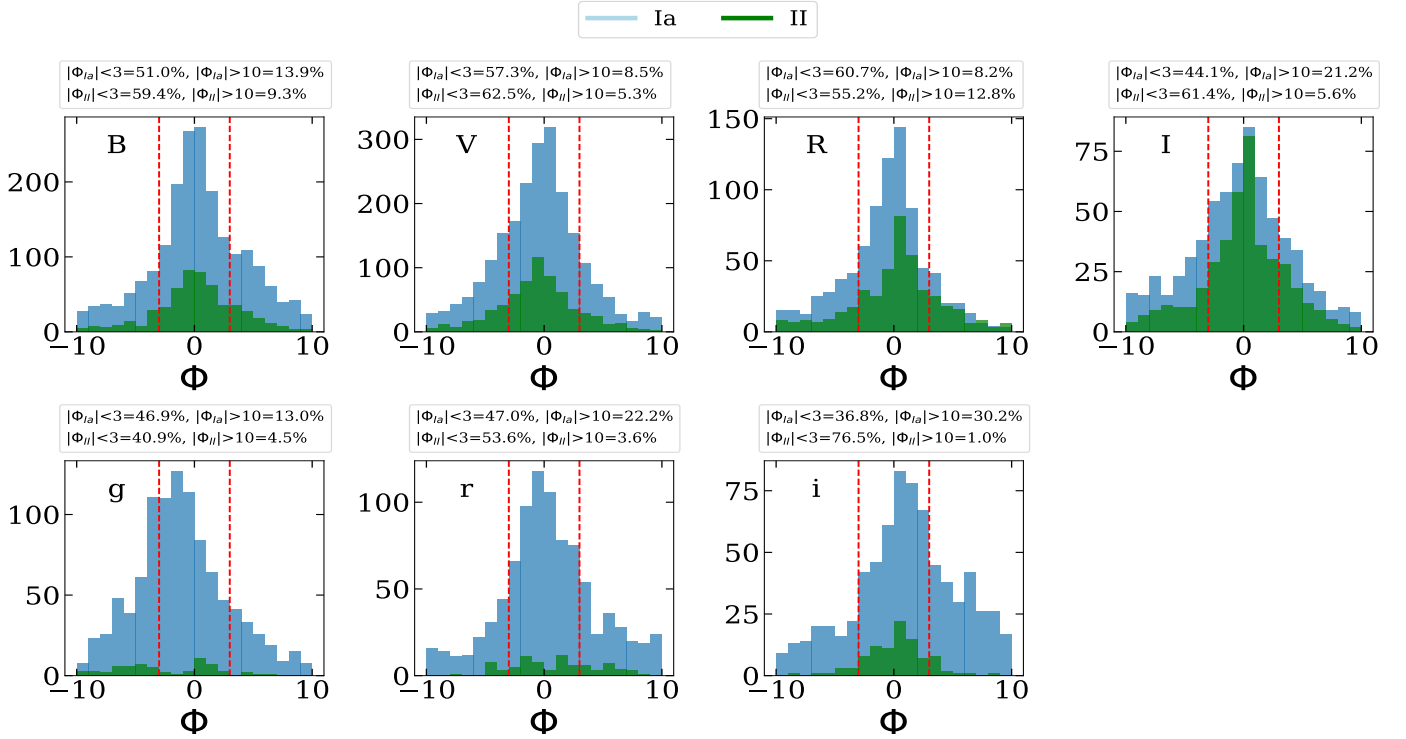


Fig. C.2. Same as Fig. C.1, but with the relative residuals computed using the leave-one-out cross-validation test.

Table C.1. SNe included in this work.

SN Name	Type	N° spec	Phase Range ^(a)	Photometry data	References ^(b)
ASASSN-14lp	Ia	8	[-13,61]	<i>UBVugri</i>	(1), (2)
SN2006le	Ia	19	[-11,35]	<i>UBVRI</i>	(79), (38), (1), (31), (14), (17), (65)
SN2007hj	Ia	17	[-4,70]	<i>BV</i>	(85), (1), (17), (14), (89), (31), (56)
SN2007cq	Ia	7	[-7,37]	<i>BVR</i>	(31), (4), (14), (17), (38), (1), (65)
SN2007ci	Ia	14	[-10,25]	<i>BVRI</i>	(14), (87), (17), (31), (1), (38)
SN2007ca	Ia	10	[0,32]	<i>BVugri</i>	(31), (59), (14), (56), (38), (17), (1), (65)
SN2007bm	Ia	14	[-10,39]	<i>BVRI</i>	(14), (4), (56), (1), (69), (38), (17), (59)
SN2007bd	Ia	12	[-9,13]	<i>BVugri</i>	(38), (59), (86), (69), (17), (56), (14), (1)
SN2007au	Ia	5	[-6,15]	<i>BVRI</i>	(14), (17), (1), (31), (38)
SN2007af	Ia	40	[-12,68]	<i>UBVRIugri</i>	(31), (59), (56), (84), (17), (83), (4), (38), (14)
SN2007S	Ia	26	[-7,32]	<i>UBVugri</i>	(14), (4), (56), (38), (59), (1), (17), (65)
SN2007F	Ia	14	[-8,53]	<i>BVRI</i>	(38), (1), (69), (88), (14), (17)
SN2007A	Ia	9	[-5,12]	<i>BVr</i>	(56), (14), (85), (1), (17), (59)
SN2006oa	Ia	7	[-12,0]	<i>UBVgriz</i>	(66), (38), (3), (14), (17), (80)
SN2006lf	Ia	19	[-9,45]	<i>BVRI</i>	(1), (14), (79), (31), (17), (38), (65)
SN2006kf	Ia	7	[-3,28]	<i>Vgr</i>	(38), (14), (17), (1), (56), (59), (78)
SN2007on	Ia	21	[-5,76]	<i>UBVugri</i>	(4), (56), (1), (59), (29)
SN2006gz	Ia	21	[-14,9]	<i>UBVri</i>	(17), (16), (14), (77)
SN2006gr	Ia	18	[-11,49]	<i>UBVRI</i>	(14), (38), (1), (31), (76), (17), (65)
SN2006et	Ia	9	[1,43]	<i>BVugri</i>	(59), (56), (38), (14), (1), (17)
SN2006cp	Ia	8	[-11,8]	<i>UBVRI</i>	(31), (38), (17), (1), (14), (73), (65)
SN2006ax	Ia	15	[-11,32]	<i>UBVugri</i>	(38), (56), (59), (14), (17), (1), (72), (65)
SN2006X	Ia	50	[-14,71]	<i>UBVRIugri</i>	(38), (31), (65), (81), (59), (82), (17), (83), (4)
SN2006S	Ia	19	[-6,20]	<i>BV</i>	(38), (1), (14), (17)
LSQ12gdj	Ia	11	[-13,48]	<i>UBVRIri</i>	(6), (7), (3), (4), (8), (9)
SN2005mz	Ia	3	[-8,11]	<i>UBV</i>	(17), (38), (14), (4)
SN2005ki	Ia	5	[0,45]	<i>UBVRIugri</i>	(14), (56), (1), (69), (17), (59), (70), (38)
SN2005kc	Ia	8	[0,13]	<i>UBVugri</i>	(59), (56), (17), (38), (1), (14)
SN2005hk	Ia	36	[-12,71]	<i>UBVRIugriz</i>	(67), (14), (65), (4), (16), (68), (17), (69), (66)
SN2005hc	Ia	6	[-3,13]	<i>Vugriz</i>	(17), (66), (38), (67), (56), (14), (1), (59)
SN2007le	Ia	48	[-12,65]	<i>BVRIugri</i>	(65), (90), (14), (56), (85), (83), (31), (59), (1), (17)
SN2007qe	Ia	13	[-11,32]	<i>BVRI</i>	(38), (14), (1), (31), (17), (65)
SN2005eq	Ia	17	[-6,55]	<i>BVRr</i>	(64), (56), (31), (59), (17), (38), (14), (1)
SN2011by	Ia	13	[-13,49]	<i>UBVRI</i>	(29), (65), (1), (3), (4), (2), (108), (69)
SN2017hbi	Ia	5	[-14,59]	<i>BVRIi</i>	(2), (1), (69)
SN2017erp	Ia	12	[-12,42]	<i>UBVRI</i>	(4), (2), (1), (69)
SN2017drh	Ia	5	[0,72]	<i>BVRI</i>	(132), (1), (2), (69)
SN2016coj	Ia	19	[-11,19]	<i>UBVRIgriz</i>	(132), (3), (133), (4), (2), (1), (69)
SN2015bp	Ia	11	[-7,30]	<i>UBV</i>	(4), (3), (131)
SN2014dg	Ia	3	[-7,17]	<i>UBV</i>	(1), (4), (2)
SN2014J	Ia	16	[-11,59]	<i>UBVRIgriz</i>	(115), (1), (128), (29), (129), (130), (120), (3)
SN2013gq	Ia	5	[-4,12]	<i>BVR</i>	(9), (2), (1), (3), (69)
SN2013dy	Ia	32	[-13,62]	<i>UBVRIgriz</i>	(55), (115), (125), (126), (2), (118), (4), (127), (1)
SN2012ht	Ia	17	[-13,77]	<i>UBVRIugri</i>	(123), (1), (29), (7), (3), (4), (2), (124), (115)
SN2012fr	Ia	46	[-15,75]	<i>UBVRIugri</i>	(118), (1), (119), (120), (2), (29), (121), (3), (122), (4)
SN2012cg	Ia	19	[-17,45]	<i>UBVRI</i>	(115), (3), (116), (83), (29), (1), (4), (2), (117)
SN2011fe	Ia	49	[-17,77]	<i>UBVRIgr</i>	(83), (109), (3), (110), (111), (112), (113), (114)
SN2009kq	Ia	3	[4,27]	<i>VRr</i>	(65), (1), (85), (2), (107), (69)
SN2008J	Ia	3	[-9,12]	<i>Vgri</i>	(95), (96), (3), (29), (97), (98)
SN2009ig	Ia	13	[-15,64]	<i>UBVRI</i>	(83), (105), (65), (106), (4), (3), (99), (2), (94)
SN2009dc	Ia	21	[-9,80]	<i>UBVRIri</i>	(29), (59), (65), (4), (3), (2), (103), (104)
SN2009ad	Ia	4	[-1,32]	<i>Vr</i>	(56), (85), (102), (65)
SN2009Y	Ia	12	[-8,64]	<i>UBV</i>	(65), (4), (1), (56), (85), (2)
SN2008s1	Ia	17	[-7,32]	<i>BV</i>	(4), (94), (17), (1), (14), (65)
SN2008hv	Ia	9	[-7,70]	<i>UBVugri</i>	(65), (4), (1), (56), (2), (59), (3), (85), (94)
SN2008fp	Ia	10	[-4,62]	<i>BVgr</i>	(56), (3), (93), (59)
SN2008ec	Ia	5	[0,43]	<i>UBVRI</i>	(1), (31), (92), (4)
SN2008bf	Ia	23	[-10,41]	<i>BVR</i>	(31), (56), (38), (1), (14), (17)
SN2008bc	Ia	7	[-5,18]	<i>BVugri</i>	(59), (56)
SN2008ar	Ia	15	[-9,48]	<i>UBVRI</i>	(91), (14), (56), (85), (1), (17), (31)
SN2008Z	Ia	13	[-8,56]	<i>UBVRri</i>	(85), (1), (101), (14), (17), (31), (65)
SN2008Q	Ia	6	[-8,-1]	<i>UBVRr</i>	(4), (14), (99), (1), (31), (85), (100), (17)
SN2005eu	Ia	6	[-9,23]	<i>BVRI</i>	(38), (1), (31), (14), (17), (65)
SN2006D	Ia	19	[-7,68]	<i>BVgr</i>	(31), (59), (74), (38), (56), (17), (14), (1), (75)

Table C.1. Continued.

SN Name	Type	N° spec	Phase Range ^(a)	Photometry data	References ^(b)
SN2005el	Ia	14	[-7,59]	BVR <i>ugri</i>	(63), (56), (31), (59), (38), (14), (1), (17)
SN2002ha	Ia	9	[-5,38]	BVRI	(14), (17), (1), (38), (31)
SN2002dp	Ia	9	[-7,42]	BVR	(14), (17), (1), (38), (31)
SN2002dj	Ia	10	[-11,13]	BVRI	(38), (14), (48), (1), (16), (17), (31)
SN2002cs	Ia	7	[-10,30]	BVRI	(17), (31), (3), (14), (47), (1)
SN2005de	Ia	4	[-2,39]	BVRI	(3), (1), (31), (47)
SN2002cf	Ia	3	[-8,13]	BVRI	(17), (31), (14), (1)
SN2002cd	Ia	13	[-9,51]	UBVRI	(1), (17), (31), (38), (14)
SN2002bo	Ia	40	[-13,72]	UBVI	(25), (17), (45), (14), (46), (31), (1)
SN2001ep	Ia	24	[-4,66]	BVRI	(14), (42), (17), (1), (38), (31)
SN2001en	Ia	10	[2,34]	BVRI	(1), (14), (31), (17), (38)
SN2001el	Ia	10	[-7,54]	BVRI	(1), (39), (40), (16), (41)
SN2001cp	Ia	9	[-8,27]	BVRI	(14), (17), (1), (3), (31), (38)
SN2001ck	Ia	3	[4,33]	BVRI	(1), (17), (14), (31)
SN2001bf	Ia	11	[0,72]	BVRI	(14), (17), (29), (1), (38), (31)
SN2001V	Ia	69	[-12,75]	UBVRI	(43), (17), (14), (1), (38), (44), (31)
SN2000fa	Ia	13	[-12,41]	UBVRI	(1), (14), (30), (17), (31)
SN2000dn	Ia	5	[-9,15]	BVRI	(1), (17), (31), (14)
SN2000dk	Ia	11	[-6,58]	BVR	(14), (17), (1), (30), (31)
SN2000cu	Ia	3	[7,39]	BVR	(1), (17), (31), (14)
SN2000cn	Ia	7	[-10,21]	UBVRI	(14), (17), (31), (1), (30)
SN1999dk	Ia	4	[-10,42]	BVRI	(1), (36), (21), (31), (37)
SN1999cp	Ia	3	[-12,13]	BVRI	(14), (34), (1), (31), (35), (17)
SN1998dm	Ia	13	[-12,48]	BVRI	(30), (17), (31), (33), (14), (1)
SN1998dh	Ia	12	[-10,70]	BVRI	(1), (30), (31), (17), (14), (32)
SN1998aq	Ia	41	[-11,77]	UBVRI	(16), (27), (1), (17), (28), (29), (14)
SN1994S	Ia	4	[-4,0]	BVR	(14), (15), (16), (17), (18), (1)
SN1994D	Ia	47	[-11,59]	UBVRI	(19), (20), (21), (1), (22), (23), (24), (25), (26)
SN1990N	Ia	3	[-1,18]	UBVRI	(1), (10), (11), (12), (13)
SN2002er	Ia	14	[-12,22]	UBVRI	(1), (49), (50), (31), (17), (51), (16), (14)
SN2002cr	Ia	8	[-10,31]	UBVRI	(14), (1), (17), (31), (38)
iPTF14bdn	Ia	7	[-19,17]	UBV	(3), (4), (5)
SN2005M	Ia	24	[-5,68]	BVR <i>Iugri</i>	(31), (59), (71), (56), (17), (38), (14), (1)
SN2004eo	Ia	20	[-12,70]	BVR <i>Iugri</i>	(31), (59), (16), (56), (61), (1)
SN2004ey	Ia	5	[-9,51]	BV <i>ugri</i>	(59), (56), (31), (1)
SN2004ef	Ia	25	[-9,58]	BVR <i>Iugri</i>	(38), (31), (59), (56), (60), (1), (14), (17)
SN2004dt	Ia	25	[-10,83]	BVR <i>Iri</i>	(56), (57), (1), (53), (3), (16), (17), (58), (14)
SN2004bv	Ia	4	[6,62]	BVRI	(1), (31), (55)
SN2004fz	Ia	4	[-9,20]	BVRI	(1), (17), (31), (14)
SN2004gs	Ia	11	[-5,30]	V _r	(14), (31), (56), (59), (62), (1), (17)
SN2003du	Ia	56	[-12,71]	UBVRI	(1), (53), (38), (54), (17), (31), (14), (16), (29)
SN2003fa	Ia	21	[-12,39]	UBVRI	(14), (1), (31), (17), (38)
SN2003cg	Ia	22	[-8,15]	UBVI	(16), (14), (52), (17), (29), (1), (31), (38)
SN2005cf	Ia	70	[-14,75]	UBVRI	(134), (38), (1), (135), (16), (31), (136), (137), (4)
SN2003Y	Ia	5	[-7,20]	BVRI	(17), (31), (14), (1)
SN2003W	Ia	8	[-9,47]	UBVRI	(14), (1), (31), (17), (38)
SN2014cy	II	6	[-120,-50]	BVR <i>Igri</i>	(9), (175), (1), (3), (145)
SN2006au	II	8	[-61,-19]	BV <i>ugri</i>	(185), (3), (187)
SN2005ay	II	8	[-106,-28]	UBVRI	(138), (3), (166), (1), (141)
SN2013ej	II	23	[-91,334]	UBVRI <i>lugriz</i>	(169), (4), (170), (171), (172), (3), (145), (9), (173), (174)
SN2006V	II	7	[-24,18]	BV <i>ugri</i>	(3), (185), (186), (187)
SN2013am	II	13	[-106,-27]	UBVRI <i>gri</i>	(170), (188), (189), (1), (4), (145), (3), (159)
SN2013ai	II	8	[-11,37]	UBV <i>gri</i>	(9), (4), (175), (3), (170)
SN2005cs	II	20	[-127,36]	UBVRI _z	(138), (139), (140), (141), (1), (4), (3), (142), (16)
SN1990E	II	4	[27,175]	BVRI	(3), (159), (176), (177), (16), (1), (178), (144)
SN1986L	II	9	[-107,-74]	BV	(143), (146), (147), (144), (148), (149)
SN1999em	II	12	[-111,-40]	UBVRI	(138), (143), (150), (1), (151), (141)
SN1999gi	II	9	[-120,16]	BVRI	(138), (165), (16), (1)
SN2002gw	II	9	[-87,-10]	BVI	(149), (143), (3), (144)
SN2004et	II	26	[-102,231]	UBVRI	(138), (16), (190), (191), (192), (193), (1), (194)
SN2006be	II	4	[-72,-39]	BV <i>ri</i>	(144), (143), (1), (166)
SN2007il	II	5	[-80,-25]	VI	(1), (144), (143), (195), (145)
SN2003T	II	3	[-85,-48]	BVI	(143), (144), (149)

SN Name	Type	N° spec	Phase Range ^(a)	Photometry data	References ^(b)
SN2007od	II	20	[-115,-72]	<i>UBVRI</i> <i>i</i>	(166), (179), (145), (143), (144), (180), (1), (4)
SN2003bn	II	7	[-103,-16]	<i>BVI</i>	(143), (144), (149)
SN2007aa	II	9	[-73,3]	<i>BVri</i>	(144), (4), (166), (143), (167), (3), (168)
SN2002bx	II	9	[-49,-17]	<i>UBVRI</i>	(138), (1), (166)
SN2008aw	II	23	[-72,6]	<i>UBVRI</i>	(4), (1), (143), (144), (145)
SN2008bj	II	8	[-103,-36]	<i>UBVri</i>	(182), (166)
SN2008bx	II	6	[-74,-4]	<i>BVR</i> <i>Iri</i>	(1), (145), (166)
SN2003gd	II	4	[-23,99]	<i>BVRI</i>	(152), (138), (153), (154), (1), (144), (143), (155), (3)
SN2003hn	II	5	[-66,32]	<i>UBVRI</i>	(143), (156), (3), (144), (47), (149)
SN2004A	II	3	[-10,69]	<i>BVRI</i>	(3), (162), (159), (163), (164), (1)
SN2004dj	II	11	[36,1125]	<i>UBVRI</i>	(3), (157), (16), (158), (1), (159), (160), (161)
SN2002hx	II	6	[-48,47]	<i>BVI</i>	(143), (144), (149)
SN2009js	II	3	[-94,-50]	<i>BVRI</i>	(1), (3), (145), (183), (184)
SN2009dd	II	10	[-105,114]	<i>UBVRI</i> <i>i</i>	(181), (3), (166)

(a) Phase range of the given SN.

(b) References: (1) Silverman et al. (2012a); (2) Stahl et al. (2020); (3) Yaron & Gal-Yam (2012); (4) Brown et al. (2014); (5) Smitka et al. (2015); (6) Walker et al. (2015); (7) Smartt et al. (2015); (8) Cellier-Holzem et al. (2012); (9) Childress et al. (2016); (10) Jeffery et al. (1992); (11) Lira et al. (1998); (12) Gómez & López (1998); (13) Mazzali et al. (1993); (14) Matheson et al. (2008); (15) Riess et al. (1999); (16) Richardson et al. (2001); (17) Blondin et al. (2012); (18) López et al. (1991); (19) Richmond et al. (1995); (20) Marshall & Severson (2022); (21) Altavilla et al. (2004); (22) Heraudeau et al. (1994); (23) Argyle et al. (1994); (24) Walker et al. (1994); (25) Panagia et al. (2006); (26) 199 (1997); (27) Riess et al. (2005); (28) Branch et al. (2003); (29) Chomiuk et al. (2016); (30) Jha et al. (2006); (31) Ganeshalingam et al. (2010); (32) Hanzl (1998); (33) Bouma et al. (1998); (34) Krisciunas et al. (2000); (35) Mukai & Ishida (1999); (36) Krisciunas et al. (2001); (37) Lee et al. (1999); (38) Hicken et al. (2009); (39) Krisciunas et al. (2003); (40) Wang et al. (2003); (41) Foley et al. (2008); (42) Sauer et al. (2008); (43) Vinkó et al. (2003); (44) Lair et al. (2006); (45) Szabó et al. (2003); (46) Krisciunas et al. (2004); (47) Harutyunyan et al. (2008); (48) Pignata et al. (2008a); (49) Pignata et al. (2004); (50) Christensen et al. (2003); (51) Kotak et al. (2005); (52) Elias-Rosa et al. (2006); (53) Leonard et al. (2005); (54) Stanishev et al. (2007); (55) Szalai et al. (2019); (56) Folatelli et al. (2013); (57) Rajala et al. (2004); (58) Altavilla et al. (2007); (59) Contreras et al. (2010); (60) Argo et al. (2004); (61) Pastorello et al. (2007a); (62) Filippenko & Foley (2004); (63) Green (2005); (64) Ponticello et al. (2005); (65) Friedman et al. (2015); (66) Sako et al. (2018); (67) Holtzman et al. (2008); (68) Sahu et al. (2008); (69) Stahl et al. (2019); (70) Lee et al. (2005); (71) Gonzalez (2005); (72) Madison et al. (2006); (73) Puckett et al. (2006); (74) Aldering et al. (2002); (75) Thomas et al. (2007); (76) Frieman et al. (2006); (77) Hicken et al. (2007); (78) Diepvens et al. (2006); (79) Frieman & Sloan Digital Sky Survey Collaboration (2006); (80) Östman et al. (2011); (81) Wang et al. (2008); (82) Yamanaka et al. (2009); (83) Johansson et al. (2017); (84) Simon et al. (2007); (85) Hicken et al. (2012); (86) Prasad & Li (2007); (87) Puckett et al. (2007a); (88) Puckett et al. (2007b); (89) Blondin et al. (2007b); (90) Simon et al. (2009); (91) Rostopchin & Westfall (2008); (92) Rex et al. (2008); (93) Pignata et al. (2008b); (94) Brown et al. (2012); (95) Fox et al. (2013); (96) Taddia et al. (2012a); (97) Silverman et al. (2013b); (98) Fox et al. (2010); (99) McClelland et al. (2013); (100) Corelli et al. (2008); (101) Puckett et al. (2008); (102) Newton et al. (2009); (103) Taubenberger et al. (2013); (104) Taubenberger et al. (2011); (105) Foley et al. (2012); (106) Navasardyan et al. (2009); (107) Gagliano et al. (2009); (108) Silverman et al. (2013a); (109) Mazzali et al. (2014); (110) Maguire et al. (2014); (111) Chomiuk et al. (2012); (112) Taubenberger et al. (2015); (113) Munari et al. (2013); (114) Pereira et al. (2013); (115) Vinkó et al. (2018); (116) Silverman et al. (2012b); (117) Graur et al. (2016); (118) Graham et al. (2017); (119) Drake et al. (2009); (120) Childress et al. (2015); (121) Childress et al. (2013); (122) Zhang et al. (2014b); (123) Burns et al. (2018); (124) Yamanaka et al. (2014); (125) Zhai et al. (2016); (126) Pan et al. (2015); (127) Zheng et al. (2013); (128) Goobar et al. (2014); (129) Foley et al. (2014); (130) Galbany et al. (2016b); (131) Srivastav et al. (2017); (132) Foley et al. (2018); (133) Zheng et al. (2017); (134) Leonard (2007); (135) Pastorello et al. (2007b); (136) Wang et al. (2009); (137) Bufano et al. (2009); (138) Faran et al. (2014); (139) Dessart et al. (2008); (140) Pastorello et al. (2006); (141) Gal-Yam et al. (2008); (142) Pastorello et al. (2009); (143) Anderson et al. (2014); (144) Gutiérrez et al. (2017); (145) de Jaeger et al. (2019); (146) Mattei et al. (1986); (147) Zanotta et al. (1986); (148) Turatto et al. (1990); (149) Galbany et al. (2016a); (150) Hamuy et al. (2001); (151) Elmhamdi et al. (2003); (152) Hendry et al. (2005); (153) Van Dyk et al. (2003); (154) Strolger et al. (2003); (155) Sugerman et al. (2006); (156) Russell et al. (2003); (157) Vinkó et al. (2006); (158) Leonard et al. (2006); (159) Silverman et al. (2017); (160) Zhang et al. (2006); (161) Vinkó et al. (2009); (162) Hendry et al. (2006); (163) Szalai & Vinkó (2013); (164) Behrend et al. (2004); (165) Leonard et al. (2002); (166) Hicken et al. (2017); (167) Doi et al. (2007); (168) Maguire et al. (2012); (169) Mauerhan et al. (2017); (170) Tinyanont et al. (2016); (171) Chakraborti et al. (2016); (172) Dhungana et al. (2016); (173) Yuan et al. (2016); (174) Valenti et al. (2014); (175) Valenti et al. (2016); (176) Schmidt et al. (1993); (177) Benetti et al. (1994); (178) Gómez & López (2000); (179) Andrews et al. (2010); (180) Inserra et al. (2011); (181) Inserra et al. (2013); (182) Yuan et al. (2008); (183) Gandhi et al. (2013); (184) Silverman et al. (2009); (185) Taddia (2012); (186) Navasardyan et al. (2006); (187) Taddia et al. (2012b); (188) Rubin et al. (2016); (189) Zhang et al. (2014a); (190) Sahu et al. (2006); (191) Li et al. (2005); (192) Maguire et al. (2010); (193) Kotak et al. (2009); (194) Fabbri et al. (2011); (195) Blondin et al. (2007a)